Computational bifurcations and stability analysis of the flow in a cubical cavity heated from below

D. Puigjaner[1], J. Herrero[2], C. Simó[3] and Francesc Giralt[2,*]

(1) Dept. Enginyeria Informàtica i Matemàtiques, ETSE, Univ. Rovira i Virgili, Tarragona, Catalunya, Spain.

(2) Dept. Enginyeria Química, ETSEQ, Univ. Rovira i Virgili, Tarragona, Catalunya, Spain.

(3) Dept. Matemàtica Aplicada i Anàlisi, Univ. de Barcelona, Barcelona, Catalunya, Spain.

(*) Corresponding author. Phone:34977559638; Fax:34977558205; e-mail:fgiralt@etseq.urv.es

Abstract

A numerical study of bifurcations and stability of the steady convective flow of air in a cubical enclosure heated from below was carried out using a Galerkin spectral method. The set of basis functions was chosen so that all boundary conditions and the continuity equation were implicitly satisfied. A parameter continuation method was applied to determine the steady solutions and bifurcations of the nonlinear governing equations as a function of Rayleigh number (Ra) for values of Ra up to 1.5×10^5. The eigenvalue problem associated with the stability analysis of the steady solutions along the different branches of solutions was solved using the Arnoldi method. The convergence of the method was consistent with the number of modes used and the results were also verified by a numerical solution of the unsteady equations of motion using a finite difference solver. Present results show that different stable convective flow patterns can coexist for different ranges of the Rayleigh number and clarify incompleteness of previous numerical results reported in the literature.

I. Introduction

Lid–driven and natural convection flows in rectangular cavities and within horizontal annuli have been widely studied because of their fundamental interest in relation to the genesis and evolution of flow patterns and the onset of unsteadiness.[1–3] As a result, these flows have been investigated for different boundary conditions and have been often employed as benchmark problems for two and three dimensional Navier–Stokes solvers.[4–6]

The most fundamental stability analyses of convection flows carried out in the past considered a fluid layer of infinite horizontal extent.[7–12] In this case, the stable flow pattern consists of straight, parallel rolls[12] and the stability regimes of these rolls as a function of the Prandtl and Rayleigh number (the "Busse balloon") are well understood.[9] Nevertheless, two-dimensional (2D) flows in plane rectangular enclosures cannot be rigorously realized in practice as side walls play an important role in finite flow configurations,[13] i.e., the end wall bias or "contamination" is unavoidable. Alternatives are to carry out three-dimensional (3D) stability studies or to consider toroidal cavities of rectangular (or circular) cross-sections[14] since they are devoid of end wall effects.

Several approaches have been used to study bifurcations and stability in convective 3D flows. One choice is time-forward integration of the non-stationary equations,[15–17] but time–marching methods are affected by the choice of initial conditions and are unable to follow the evolution of unstable solutions that could lead to stable ones at subsequent bifurcations. Unlike direct time-marching calculations, numerical bifurcation and parameter continuation methods detect more effectively critical points and their variation with relevant parameters.[5,6,18–20]

The first bifurcation for the transition from the motionless conductive state to the onset of convection is well documented in the literature for 2D rectangular cavities and for 3D enclosures with a variety of width/height and length/height aspect ratios (h_1, h_2).[7,8,10,11,13,21] The aim of the present study is to analyze the bifurcations and stability of steady convective flow patterns of air ($Pr = 0.71$) in a cubical cavity heated from below up to a Rayleigh number of $Ra = 1.5 \times 10^5$. Because of the intrinsic symmetry of the cubical geometry this natural convection flow tends to produce state solutions with manifold symmetries. As the Rayleigh number is increased, new bifurcations of the steady convective solutions are prone to occur so that the flow is expected to generate a rather complex bifurcation diagram. Recent experimental[22] and numerical[15,17] studies report a variety of steady stable patterns at moderate Rayleigh numbers. Only two of these flow patterns could be confirmed following the pioneer linear stability analysis of Catton.[23]

The aim of the present study is to extend previously published works by first completing the divergence-free basis functions proposed by Catton[23] and, second, by determining the bifurcation diagram of the flow. The bifurcation diagram displays the stability and domains of existence of the alternative steady solutions that arise at bifurcation points. Both stable and unstable branches are followed using a parameter continuation algorithm applied to the nonlinear steady governing equations. The solutions of the governing equations are obtained by means of a Galerkin method with divergence–free basis functions. At any steady solution along the different bifurcating branches the stability of the flow is studied by linearizing the governing equations around that solution. Thus, the method extends the analysis beyond the regions around bifurcation points. Unstable flow patterns are also considered because they can become stable as a consequence of subsequent bifurcations.

II. Physical model and governing equations

The calculation domain scaled by the length of the side of the cubical cavity, L, is given by $\Omega = [-\frac{1}{2}, \frac{1}{2}] \times [-\frac{1}{2}, \frac{1}{2}] \times [-\frac{1}{2}, \frac{1}{2}]$. The temperatures at the top and the bottom horizontal walls are constant and equal to T_c and T_h, respectively. The Boussinesq approximation of the governing equations is assumed. The characteristic scales for velocity, temperature, time and pressure are $q_0 = [\beta(\Delta\theta)gL\alpha/\nu]^{\frac{1}{2}}$, $\Delta\theta$, L^2/α and $\rho\nu q_0/L$, respectively, where ρ is the density of the fluid, g is the acceleration of gravity, $\Delta\theta = \mathrm{T}_h\text{-}\mathrm{T}_c$, β is the coefficient of thermal expansion, ν is the kinematic viscosity and α is the thermal diffusivity. Using these scales the governing dimensionless nonlinear equations for the velocity $\vec{V} = (u, v, w)$, the temperature departure from the motionless conductive state, θ, and the pressure, p, are

$$\frac{1}{Pr}\left(\frac{\partial \vec{V}}{\partial t} + Ra^{\frac{1}{2}}(\vec{V}\cdot\nabla)\vec{V}\right) - \nabla^2\vec{V} - Ra^{\frac{1}{2}}\theta\,\vec{e_z} + \nabla p = 0\,, \tag{1}$$

$$\frac{\partial \theta}{\partial t} + Ra^{\frac{1}{2}}(\vec{V}\cdot\nabla)\theta - \nabla^2\theta - Ra^{\frac{1}{2}}w = 0\,, \tag{2}$$

$$\nabla\cdot\vec{V} = 0\,. \tag{3}$$

The Rayleigh number and the Prandtl number are defined as $Ra = \beta(\Delta\theta)gL^3/\alpha\nu$ and $Pr = \nu/\alpha$, respectively, and $\vec{e_z}$ denotes the unit vector in the z direction.

It is assumed that the six walls of the cavity are rigid and the four lateral walls are adiabatically insulated. The corresponding boundary conditions are

$$\vec{V} = \theta = 0 \text{ on } |z| = \frac{1}{2}, \quad \vec{V} = \frac{\partial\theta}{\partial x} = 0 \text{ on } |x| = \frac{1}{2}, \quad \vec{V} = \frac{\partial\theta}{\partial y} = 0 \text{ on } |y| = \frac{1}{2}. \tag{4}$$

III. Numerical Procedure

A. Galerkin method

A Galerkin method[24] with globally defined basis functions was used to determine the bifurcations and stability of the steady solutions of equations (1-3) subject to boundary conditions (4). The set of basis functions was chosen so that all boundary conditions and the continuity equation were implicitly satisfied. The advantage of this choice is that the projection of the pressure gradient onto the basis is analytically zero, which means that pressure gradient is not present in the final equations.

In order to get a set of divergence-free basis functions to expand the velocity field it is convenient to represent the solenoidal velocity vector field $\vec{V}$ by means of two scalar potentials[13,25]

$$\vec{V} = \nabla \times (\hat{\Phi}^{(1)}\vec{e}_x) + \nabla \times (\hat{\Phi}^{(2)}\vec{e}_y) = \left(-\frac{\partial \hat{\Phi}^{(2)}}{\partial z}, \frac{\partial \hat{\Phi}^{(1)}}{\partial z}, \frac{\partial \hat{\Phi}^{(2)}}{\partial x} - \frac{\partial \hat{\Phi}^{(1)}}{\partial y} \right), \tag{5}$$

where $\vec{e}_x$ and $\vec{e}_y$ are the unit vectors in x and y directions, respectively, and $\hat{\Phi}^{(1)}$ and $\hat{\Phi}^{(2)}$ are scalar functions. When equation (5) is used to describe the velocity field the boundary conditions for $\hat{\Phi}^{(1)}$ and $\hat{\Phi}^{(2)}$ are

$$\begin{aligned} u &= -\frac{\partial \hat{\Phi}^{(2)}}{\partial z} = 0, \\ v &= -\frac{\partial \hat{\Phi}^{(1)}}{\partial z} = 0, \\ w &= -\frac{\partial \hat{\Phi}^{(2)}}{\partial x} - \frac{\partial \hat{\Phi}^{(1)}}{\partial y} = 0. \end{aligned} \tag{6}$$

Pallares et al.,[26] used the uncoupled boundary conditions

$$\frac{\partial \hat{\Phi}^{(2)}}{\partial x} = \frac{\partial \hat{\Phi}^{(1)}}{\partial y} = 0 \tag{7}$$

instead of the third equation in (6) to perform a linear stability analysis in a cubical cavity heated from below. Later, Gelfgat[5] used the same uncoupled boundary conditions (7) to study the linear stability of the Rayleigh-Bénard flow in rectangular enclosures. It should be noted that boundary conditions (7) are not general[25] since some solutions fulfilling (6) in the whole domain may not satisfy the more constraining equation (7). Following Kessler,[13] the coupling of the two scalar potentials $\hat{\Phi}^{(1)}$ and $\hat{\Phi}^{(2)}$ is avoided by the addition of a scalar function $\Phi^{(3)}$ which satisfies

$$\begin{aligned} \hat{\Phi}^{(1)} &= \Phi^{(1)} + \frac{\partial \Phi^{(3)}}{\partial x}, \\ \hat{\Phi}^{(2)} &= \Phi^{(2)} + \frac{\partial \Phi^{(3)}}{\partial y}. \end{aligned} \tag{8}$$

As it is shown below, the use of equations (8) to uncouple potentials at the boundaries not only preserves mathematical consistency but has a great impact in the accuracy of the calculations. Using this extended formulation, the solenoidal velocity field is given by

$$\vec{V} = \left(-\frac{\partial}{\partial z}\left(\Phi^{(2)} + \frac{\partial \Phi^{(3)}}{\partial y}\right), \frac{\partial}{\partial z}\left(\Phi^{(1)} + \frac{\partial \Phi^{(3)}}{\partial x}\right), \frac{\partial \Phi^{(2)}}{\partial x} - \frac{\partial \Phi^{(1)}}{\partial y}\right) \tag{9}$$

with uncoupled boundary conditions

$$\frac{\partial \Phi^{(1)}}{\partial z} = \frac{\partial \Phi^{(2)}}{\partial z} = \frac{\partial \Phi^{(1)}}{\partial y} = \frac{\partial \Phi^{(2)}}{\partial x} = \frac{\partial^2 \Phi^{(3)}}{\partial z \partial x} = \frac{\partial^2 \Phi^{(3)}}{\partial z \partial y} = 0. \tag{10}$$

The basis functions chosen to expand $\Phi^{(1)}$, $\Phi^{(2)}$, $\Phi^{(3)}$, and θ satisfy boundary conditions (4) and (10) exactly. These expansions are

$$\Phi^{(1)} = \sum_{i,j,k} a^{(1)}_{ijk} g_i(x) f_j(y) f_k(z), \tag{11}$$

$$\Phi^{(2)} = \sum_{i,j,k} a^{(2)}_{ijk} f_i(x) g_j(y) f_k(z), \tag{12}$$

$$\Phi^{(3)} = \sum_{i,j,k} a^{(3)}_{ijk} f_i(x) f_j(y) h_k(z), \tag{13}$$

$$\theta = \sum_{i,j,k} a^{(4)}_{ijk} h_i(x) h_j(y) g_k(z), \tag{14}$$

where f, g and h are functions that satisfy $f(-1/2) = f(1/2) = f'(-1/2) = f'(1/2) = 0$, $g(-1/2) = g(1/2) = 0$ and $h'(-1/2) = h'(1/2) = 0$. In the present work the functions g and h used are trigonometric functions while the functions f are the so-called beam-functions,[27]

$$\begin{aligned}
g_k(x):&\quad \cos((2k-1)\pi x) \quad \text{or} \quad \sin(2k\pi x),\\
h_k(x):&\quad \cos(2(k-1)\pi x) \quad \text{or} \quad \sin((2k-1)\pi x),\\
f_k(x):&\quad C_k(x) = \frac{\cosh(\lambda_k x)}{\cosh(\lambda_k/2)} - \frac{\cos(\lambda_k x)}{\cos(\lambda_k/2)}\\
&\quad \text{or}\\
&\quad S_k(x) = \frac{\sinh(\mu_k x)}{\sinh(\mu_k/2)} - \frac{\sin(\mu_k x)}{\sin(\mu_k/2)}.
\end{aligned} \tag{15}$$

In expressions (15) the parameters λ_k and μ_k are the positive roots of the equations $\tanh(\lambda_k/2) + \tan(\lambda_k/2) = 0$ and $\tanh(\mu_k/2) - \tan(\mu_k/2) = 0$, respectively.

When expansions (11-13) are substituted into expression (9) and truncated to some orders N_x, N_y, N_z, the velocity and temperature fields can be approximated by

$$\begin{pmatrix} \vec{V} \\ \theta \end{pmatrix} = \sum_{i=1}^{N_x} \sum_{j=1}^{N_y} \sum_{k=1}^{N_z} \left[a^{(1)}_{ijk} \vec{G}^{(1)}_{ijk} + a^{(2)}_{ijk} \vec{G}^{(2)}_{ijk} + a^{(3)}_{ijk} \vec{G}^{(3)}_{ijk} + a^{(4)}_{ijk} \vec{G}^{(4)}_{ijk} \right]. \tag{16}$$

where $a_{ijk}^{(l)}$, $l = 1, \cdots, 4$ are the unknown time–dependent coefficients, and $\vec{G}_{ijk}^{(l)}$, $l = 1, \cdots, 4$ are defined as

$$\vec{G}_{ijk}^{(1)}(x,y,z) = \begin{pmatrix} 0 \\ g_i(x)f_j(y)f_k'(z) \\ -g_i(x)f_j'(y)f_k(z) \\ 0 \end{pmatrix}, \quad \vec{G}_{ijk}^{(2)}(x,y,z) = \begin{pmatrix} f_i(x)g_j(y)f_k'(z) \\ 0 \\ -f_i'(x)g_j(y)f_k(z) \\ 0 \end{pmatrix},$$
$$\vec{G}_{ijk}^{(3)}(x,y,z) = \begin{pmatrix} f_i(x)f_j'(y)h_k'(z) \\ -f_i'(x)f_j(y)h_k'(z) \\ 0 \\ 0 \end{pmatrix}, \quad \vec{G}_{ijk}^{(4)}(x,y,z) = \begin{pmatrix} 0 \\ 0 \\ 0 \\ h_i(x)h_j(y)g_k(z) \end{pmatrix}. \tag{17}$$

Functions g, h and f defined in equations (15) are either even or odd functions with respect to the planes $x = 0$, $y = 0$ and $z = 0$. Since boundary conditions are symmetric with respect to these planes, a steady solution may not need all of the possible combinations between odd and even functions. The tensor products of the basis functions are classified in eight classes according to the parity with respect to the coordinates x, y and z:

$$\begin{array}{llll} \text{class 1: OEE,} & \text{class 2: OOE,} & \text{class 3: EEE,} & \text{class 4: EOE,} \\ \text{class 5: OEO,} & \text{class 6: OOO,} & \text{class 7: EEO,} & \text{class 8: EOO.} \end{array} \tag{18}$$

The three letters of each class in expressions (18) refer to the parity (O=odd, E=even)[20] of the functions used to expand the temperature θ with respect to the x, y and z axes, respectively. Thus, each of the tensor products in equations (11)-(14) and (17) actually symbolizes eight different terms.

Since for any given solution the symmetry classes of the different variables will not coincide, it is important to group them consistently. Eight symmetry blocks are defined by grouping in the i-th block the i-th symmetry classes for θ, $\partial\Phi^{(1)}/\partial y$, $\partial\Phi^{(2)}/\partial x$, and $\partial^2\Phi^{(3)}/\partial x\partial y$. In any given block the symmetry classes of w and θ coincide while the symmetry class of u can be obtained from that of w by changing the parity of basis functions with respect to x and z. The symmetry class of v is in turn obtained from that of w by changing the parity of basis functions with respect to y and z. This is summarized in Table I where all symmetry classes associated with each block are listed. As the parity of basis functions associated with each class determines which type of roll is involved, the knowledge of the classes associated with the eigenvalue whose real part has changed sign provides some preliminary information on the convective pattern near a bifurcation point. It was found that some steady solutions belong to subspaces generated by only two or four symmetry blocks. In those cases the dimension of the problem was reduced by a factor of four or two, respectively.

The three subscripts and the four superscripts in equations (16) can be collapsed into a single one for the sake of clarity,

$$\begin{pmatrix} \vec{V} \\ \theta \end{pmatrix} = \sum_{i=1}^{K} c_i \vec{F}_i, \tag{19}$$

where the vector $\vec{F}_i$ represents the complete set of three-dimensional tensor products normalized with respect to the L_2 norm. Coefficients c_i are the unknowns and $K = 32(N_x \times N_y \times N_z)$ is the total number of basis functions used. It should be mentioned that those basis functions $G^{(3)}_{ijk}$ that are well approximated by linear combinations of basis functions in the subset $\{G^{(1)}_{ijk} \cup G^{(2)}_{ijk}\}$ are omitted in the calculations. This results in a reduction of approximately 20% in the number of basis functions.

B. Continuation method

Application of the Galerkin method with expansion (19) reduces the nonlinear problem (1-2) to a system of ordinary differential equations (ODE's) that can be written as

$$B_{ji}(Pr)\frac{dc_i(t)}{dt} = L_{ji}(Ra)c_i(t) - Ra^{\frac{1}{2}} Q_{jin}(Pr)c_i(t)c_n(t), \qquad j = 1, \cdots, K\,. \tag{20}$$

if the summation convention on repeated indices is adopted. The elements of the vector $\vec{c} = (c_1, c_2, \cdots, c_K)$ are the unknowns and the matrices with components L_{ji} and Q_{jin} contain the coefficients of the linear and nonlinear terms of equation (20), respectively. The mass matrix B_{ji} contains the time derivative terms. The precise forms of matrices L, Q and B are given in the Appendix.

The left hand side of equation (20) is set to zero when computing a steady solution and the problem reduces to the set of algebraic equations

$$f_j(Pr, Ra, \vec{c}) := L_{ji}(Ra)c_i - Ra^{\frac{1}{2}} Q_{jin}(Pr)c_i c_n = 0, \qquad j = 1, \cdots, K\,. \tag{21}$$

Provided that at least one solution of equation (21) has been determined, a predictor-corrector parameter continuation method[28,29] can be used to calculate further solutions. The Rayleigh number was taken as the continuation parameter in the current study for a fixed $Pr = 0.71$. The predictor step was based on a cubical polynomial extrapolation.[29] At the corrector step the linear system to be solved in each Newton iteration, to go from iterate $\vec{c}^{(k)}$ to iterate $\vec{c}^{(k+1)}$, was

$$D_c f(Pr, Ra, \vec{c}^{(k)})(\vec{c}^{(k+1)} - \vec{c}^{(k)}) = -f(Pr, Ra, \vec{c}^{(k)}), \tag{22}$$

where $D_c f(Pr, Ra, \vec{c}^{(k)})$ is the Jacobian evaluated on $\vec{c}^{(k)}$ for given values of Ra and Pr.

The parameter continuation method was initiated with a guess solution which set in at a bifurcation point. More details about the method used for determining one solution on the emanating branch of solutions at a bifurcation point, which is also called branch switching, are given in the next section. An arclength-continuation method[30] was used in those solution branches where the parameter continuation method described above failed because of the presence of a turning point.

C. Stability analysis, bifurcations and branch switching

The linear stability of a steady solution $\vec{c}_0$ for a fixed value of the Rayleigh number Ra_0 was determined first by considering a perturbation $\vec{c}_p$

$$\vec{c} = \vec{c}_0 + e^{\sigma t}\vec{c}_p \tag{23}$$

which satisfies the continuity equation and the boundary conditions, and secondly by linearizing equation (20). The linearized equations for $\vec{c}_p$ lead to the generalized eigenvalue problem

$$\vec{c}_p = \sigma D_c f(Pr, Ra_0, \vec{c}_0)\vec{c}_p \,. \tag{24}$$

In this equation $D_c f(Pr, Ra_0, \vec{c}_0)$ is the Jacobian of the right-hand side of equation (20) evaluated at $(Pr, Ra_0, \vec{c}_0)$ and σ denotes the eigenvalues.

The linear stability of a solution $\vec{c}$ changes when one ore more eigenvalues σ cross the imaginary axis. The values of the Rayleigh number at which the real part of one or more eigenvalues σ changes sign become bifurcation points. At a bifurcation point a new convective flow pattern (or, occasionally, several flow patterns) sets in, i.e., a new branch of solutions emanates. The flow pattern that sets in at a bifurcation point will be steady if the eigenvalue σ_c that crosses the imaginary axis is real. Otherwise the eigenvalue σ_c is pure imaginary and the bifurcation corresponds to a Hopf bifurcation. In the present work, bifurcations from the motionless conductive state are referred to as primary bifurcations and the term secondary bifurcations refers to those from convective flow solutions.

Whenever a steady bifurcation was detected, first the secant method was used to determine the value Ra_0 where it occurred. Second, the solution $\vec{c}_0$ associated with the bifurcation parameter Ra_0 was calculated and finally a branch switching method[29] was used to obtain a guess solution on the emanating branch. This guess solution served as starting point to the continuation method for tracking the new branch of solutions. The branch switching method was based on a predictor that used the eigenvector $\vec{h}_0$ associated with the zero eigenvalue of the Jacobian at the bifurcation point $(Ra_0, \vec{c}_0)$. Thus, the symmetry properties of the solution $\vec{c_0}$ and of the eigenvector $\vec{h_0}$ were used to predict the symmetry properties of solutions in the emanating branch. This feature was exploited to reduce the number of basis functions involved and consequently the dimension of the set of algebraic equations (21).

Those solutions that were unstable when they set in were also taken into account because they could become stable as a consequence of a subsequent bifurcation. The Arpack implementation[31] of the Arnoldi method was used to find the eigenvalues of equation (24) with the largest real part, i.e., the leading eigenvalues. Because of computational costs, the stability analysis was only performed for those values of Ra that were multiple of 10^3 during the continuation along any branch. Notwithstanding, it was checked that eigenvalues changed smoothly with respect to the continuation parameter Ra, i.e., undesired jumpings between solution branches did not take place.

D. Accuracy assessment

1. Convergence with respect to the truncation parameters

The bifurcation Rayleigh numbers were used as a criterion for the convergence of the method with respect to the truncation parameters N_x, N_y, N_z in expansions (16). Table II presents the calculated values of the Rayleigh number at which bifurcation from the conductive state occurs for three of the solutions branches discussed in the next section. Convergence is satisfactory for the three prototypical structural topologies chosen for this test since differences between the $N_{xyz} = N_x = N_y = N_z = 5$ and $N_{xyz} = 8$ predictions are always smaller than 0.13%. The results in Table II also indicate that an increase from $N_{xyz} = 7$ to $N_{xyz} = 8$ causes at most a 0.02% change in the bifurcation value Ra_0. One can even extrapolate the data in Table II to $N_{xyz} = \infty$ by using a law of the form $a + b/N_{xyz}$. The corresponding values for the three structures $S1$, $S5$ and $S4$ are $Ra_0 \simeq 3,389$, $5,901$ and $7,456$, respectively. The differences between the $N_{xyz} = 7$ data and the extrapolated ones are below 0.06% in all cases. As a consequence, the truncation value $N_{xyz} = N_x = N_y = N_z = 7$ was employed for current calculations.

To assess the rate of convergence of expansions (19), i.e., the behavior of spectral coefficients with respect to the truncation parameter N_{xyz}, Figure 1 shows the logarithm of the absolute values of the spectral coefficients of the x–roll flow pattern at $Ra = 1.5 \times 10^5$. For the sake of clarity, only spectral coefficients associated with the basis functions used to expand temperature are plotted. A global spherical frequency $ns = \sqrt{(i^2 + j^2 + k^2)}$, where i, j and k denote the indexes associated with the three dimensional tensor products of basis functions, is used as abscissa. This figure shows the decaying behavior of the spectral coefficients for the truncation value $N_{xyz} = 7$. Note that the decay of the coefficients with increasing ns in Figure 1 approaches reasonably well the geometrical convergence behavior with a linear correlation coefficient $r = -0.87$, suggesting analyticity of the solution. The same linear correlation coefficient was obtained when the coefficients were fitted to a function of the form $Ce^{-\rho_1 i}e^{-\rho_2 j}e^{-\rho_3 k}$.

2. Boundary conditions

It is necessary to assess whether or not the simpler equation (7) might be used instead of the more demanding decoupling treatment of equations (8). Note that the addition of the third potential function implies the presence of the subset $\vec{G}^{(3)}_{ijk}$ in equation (17), with a considerable increase in the size of the problem. In fact, once a separation of variables in the form of expansions (11) and (12) is assumed, and regardless of the particular form of the functions f, g and h used in these expansions, it can be easily proved that equation (5), first and second equations in (6) and equation (7) imply that

$$\begin{aligned} \int_{z=-0.5}^{z=0.5} u\,(x,y,z)dz = 0 \\ \int_{z=-0.5}^{z=0.5} v\,(x,y,z)dz = 0 \end{aligned} \qquad \forall\,(x,y) \in \Omega\,. \tag{25}$$

These conditions pose no special problems in linear analyses[5,26] because solutions of the equations linearized around the conductive state possess a lot of symmetries, as shown in the next section. However, it is found that supercritical solutions of the nonlinear problem obtained with the proper boundary conditions (10) do not fulfill equation (25). Figures 2(a-c) show that this point is essential even for the simple x–roll structure. The calculation performed without the subset $\vec{G}^{(3)}_{ijk}$, i.e., assuming boundary conditions (7), not only overpredicts Nu by up to 5% but it underpredicts the value of Ra where $S1$ becomes unstable by as much as 44%. Note that in the absence of $\vec{G}^{(3)}_{ijk}$ in the basis (17) the Galerkin method generates a projection of the solution into the subspace of solutions fulfilling equation (7). The shortcomings of the calculations with the simplified basis are even more evident when comparing the corresponding eigenspectrums of Figures 2(b) and 2(c). Similar or even larger discrepancies in the computed eigenspectrum and Nusselt numbers were detected for other solutions of the nonlinear problem investigated when they were not computed with the complete basis.

IV. Results and discussion

A. Bifurcation diagram

Figures 3(a) and 3(b) present the bifurcation diagram for air ($Pr = 0.71$). Stable flow patterns are depicted with solid lines, while unstable flow patterns are represented by dashed lines when they have exactly one unstable eigenvalue, i.e., one eigenvalue with positive real part, and by dotted lines when they have two or more unstable eigenvalues. Steady, Hopf and saddle-node bifurcation points are marked with filled circles, hollow circles and hollow squares respectively. The solutions are labelled following the notation of Pallares et al.[15] who reported seven stable solutions, denoted as $S_i, \;\; i = 1, \cdots, 7$, in the region $Ra \leq 6 \times 10^4$. Most of the branches in Figure 3 were started by applying the branch switching method described in Section IIIC to bifurcations from the conductive state. Those convective flow patterns that set in at primary bifurcations and that had at most three unstable eigenvalues near the bifurcation point were tracked using the continuation method. Secondary bifurcations were identified and steady flow patterns that emanate at those bifurcations and that had at most two unstable eigenvalues near the bifurcation point were continued. The solutions labelled $S4$ and $S6$ are exceptions to this rule. Although these solutions have three unstable eigenvalues when they set in, they were included in the bifurcation diagram because they were reported previously in the literature.

Figure 3(a) shows the variation of the Nusselt number as a function of Ra. The flow patterns that are stable over a range of Rayleigh numbers in the region $Ra \leq 1.5 \times 10^5$ and those that, being unstable, have been previously reported in the literature, are depicted in this Figure. The rest of steady flow patterns identified are shown in Figure 3(b). For the sake of clarity the variable $Nu - 0.01Ra^{\frac{1}{2}}$ is used as ordinate instead of the Nusselt number Nu in Figure 3(b). The variation of the real part of the leading eigenvalue, i.e, the eigenvalue with the largest real part, associated with the stability analysis is depicted in Figure 4 for most of the flow patterns identified. The ranges of Ra where solutions are stable and unstable are summarized in Table III.

The bifurcation diagrams depicted in Figure 3 show a stable solution labelled as $S8$ for which no connection with any other branch originated from the conductive state has been found up to now. It is known[29] that continuation methods do not guarantee that all possible solutions can be identified. Chances to detect isolated branches are small indeed. Thus, this $S8$ solution branch, which was not identified by the continuation method, was initialized from the projection of a discrete field, calculated by a fourth-order finite difference solver on a $41 \times 41 \times 41$ uniform mesh, onto the space of basis functions described in Section IIA. Once the projection was used as a starting guess, the branch was built by the parameter continuation procedure. From the stability analysis it may be concluded that this $S8$ solution sets in as a consequence of a saddle-node bifurcation that also originates an unstable solution denoted as $S9$. In order to clarify this bifurcation, this isolated branch is also included in Figure 3(b).

1. Symmetry properties of flow patterns

Table III summarizes the main features of all flow patterns identified. Special attention has been paid to identify the group of symmetries and the group of antisymmetries of every solution. A 3×3 matrix representation is used to describe any element of these groups. Thus, if R belongs to the symmetry group of a flow pattern S then the transformations $R\vec{X}$ and $R\vec{V}$ with $\vec{X} = (x, y, z)$, $\vec{V} = (u, v, w)$ and R a 3×3 matrix do not change the flow pattern S. When R belongs to the antisymmetry group of a flow pattern S, the transformations $R\vec{X}$ and $-R\vec{V}$ must be applied to recover the original flow pattern. For instance, a rotation of angle π around the z-axis and a reflection with respect to the $x = 0$ plane are represented respectively by the following matrices R_1 and R_2,

$$R_1 = \begin{pmatrix} -1 & 0 & 0 \\ 0 & -1 & 0 \\ 0 & 0 & 1 \end{pmatrix}, \quad R_2 = \begin{pmatrix} -1 & 0 & 0 \\ 0 & 1 & 0 \\ 0 & 0 & 1 \end{pmatrix}. \tag{26}$$

A basis of the groups of symmetries and antisymmetries is given in Table III for all solutions of the nonlinear problem reported in this work, and in Table IV for solutions of the linearized problem around the conductive state. Solutions of the linearized problem around the conductive state do have antisymmetry groups while solutions of the nonlinear problem do not. Note that some or all of the elements in the symmetry groups of Table IV become redundant because they can be expressed as the product of two of the corresponding antisymmetry elements. Since some steady solutions belong to subspaces generated by only two or four symmetry blocks (see Section IIIA for definition of the symmetry block), this information is also included in Tables III and IV. It is remarkable that most flow patterns are realizable in more than one particular solution as a consequence of their symmetry properties. For example, the $S1$ solution listed in Table III takes the shape of an x–roll. The corresponding y–roll solution is obviously equally realizable and, in addition, in either case the x– or y–vorticity can take a positive or a negative sign. Thus, the $S1$ flow pattern can be realized in four different particular solutions. In this regard, it should be noted that the symmetry groups for the $S1$, $S2$ and $S5$ flow patterns given in Table III correspond to just one of the particular solutions; other realizable solutions for these three patterns might have different symmetry groups.

2. Finite difference results

The finite difference solutions of equations (1-3) were obtained by means of an explicit time-marching procedure (details are given elsewhere[34]). In the present work each particular time-marching calculation began either by continuing from a previous one at a different value of Ra or by initialization from a motionless field with a temperature distribution either uniform (hot, cold or bulk) or linear in z. Although this time-marching procedure can only provide a qualitative approximation to the bifurcation diagram, it is interesting to note that all of the stable solutions in Figure 3 were also detected in the finite difference calculations within consistent ranges of Ra, as shown in Figure 5. The solutions of type $S2$ were found in the time-marching calculations only as a temporary metastable pattern that eventually evolved towards a steady $S1$ solution. This is coherent with the current stability analysis because it shows that the only positive eigenvalue for $S2$ is close to zero at low Rayleigh numbers, i.e., $S2$ is close to being stable. Concerning the $S8$ branch, the lowest value of Ra at which the $S8$ finite difference solution was obtained is $Ra = 78,000$. If the Rayleigh number is then diminished by 1,000 units, the $S8$ pattern vanishes and the flow evolves towards a $S5$ solution.

The differences in Nusselt number between Galerkin solutions (Figure 3(a)) and time-marching solutions (Figure 5) are on the average within 1%, with a maximum deviation of 2.4% for $S7$ at $Ra = 1.5 \times 10^5$. When the mesh in the time-marching finite-difference solver was increased from $41 \times 41 \times 41$ to $81 \times 81 \times 81$ the predicted Nusselt number changed within 0.2%. Since the Nusselt number is a dimensionless temperature gradient on the wall more terms in the expansion (14) for temperature would be needed to reduce the small differences in Nu observed between Figures 3(a) and 5. However, as shown in Table II, this truncation has even milder effects on the predicted stability diagram, i.e., the flow patterns identified in the current study.

Let ρ_θ be the angle between the temperature field over a $41 \times 41 \times 41$ uniform mesh obtained by the Galerkin continuation method and by the time-marching method, respectively; $\rho_{\vec{V}}$ is defined analogously for the velocity field. Table V shows the cosine of the angles ρ_θ and $\rho_{\vec{V}}$ for stable flow patterns near the highest Ra where the flow patterns are stable. All these cosines are higher than 0.999, both for temperature and velocity. This is a good indication of the consistency and robustness of current results from the stability point of view.

Moreover, the time-marching code also detects the presence of time-periodic solutions with an structure of the x–roll type for values of the Rayleigh number larger than $Ra = 1.2 \times 10^5$, labelled as oscillating $S1$ in Figure 5. This seems to indicate that the initially unstable branch originated by a Hopf bifurcation of $S1$ at $Ra \simeq 95,000$ in Figure 3(a) might stabilize at a higher Rayleigh number. The present work is restricted to the analysis of steady solutions. The study of time-dependent solutions that arise as a result of a Hopf bifurcation will be the subject of a future work.

3. Discrepancies between present and previous results

Pallares et al.[15] reported the presence of up to seven stable solutions, denoted as $S_i,\ i = 1, \cdots, 7$, for $Pr = 0.71$ in the region $Ra \leq 6 \times 10^4$. Within this region of low Rayleigh numbers, the bifurcation diagram of Figure 3(a) does not agree with the one presented by Pallares et al. in several points. No evidence was found in the present study of the solution branch $S3$. When the continuation method was initialized from the projection of the discrete velocity and temperature fields corresponding to a $S3$ flow pattern onto the space of basis functions it converged towards $S1$. Moreover, the solutions $S2$, $S4$ and $S6$ are unstable in the whole range of Ra investigated whereas Pallares et al.[15] reported ranges of stability for these three flow structures of $3,500 \leq Ra \leq 10,000$, $8,000 \leq Ra \leq 10,000$ and $15,000 \leq Ra \leq 60,000$, respectively. In addition, these authors[15] suggested some wrong connections between solution branches, probably because of a misinterpretation of what they referred to as flow transitions. When a stable solution disappears after an increase in Ra, the resulting solution given by a time-marching code is not necessarily the solution being actually originated as a result of the bifurcation. In this context, the preferred steady solution is the stable solution with the largest basin of attraction in the space of initial states of the system. The study of the basin of attractions of the steady solutions identified in the present work will be the subject of a future work.

B. Bifurcations from the conductive state

1. Flow patterns near bifurcations

The linear stability analysis of the Rayleigh-Bénard problem performed by Catton[23] in a cubical cavity produced the critical Rayleigh number at $Ra_c = 3,446$ and the resulting mode was of the x– or y–roll type. The present study predicts that the critical Rayleigh number is $Ra_c = 3,389$, as shown in Table II. This critical value corresponds to a double eigenvalue, indicating that any linear combination of the two eigenvectors, i.e., of one x–roll and one y–roll, is possible according to stability analysis. Nevertheless, among all possible combinations, only a stable single x– or y–roll and an unstable diagonal $x \pm y$–roll are found when applying the branch switching method described in Section IIIC.

The stable flow pattern $S1$ drawn in Figure 6(a) is formed by one x–roll. The unstable flow pattern $S2$ also originated at $Ra_c = 3,389$ is a single–roll but with a diagonal mode of circulation, as shown in Figure 6(b). At slightly supercritical Rayleigh numbers the $S2$ solution is essentially obtained by subtracting one x–roll from one y–roll. In a similar way, a symmetric solution is found by adding them. These two flow patterns were already numerically predicted by Ozoe et al.[32] At the second primary bifurcation ($Ra \simeq 5,902$) an initially unstable flow pattern named $S5$ is developed, as indicated in Tables II and III. This second primary bifurcation cannot be predicted by the incomplete set of functions proposed by Catton.[23] At slightly supercritical Rayleigh numbers, the $S5$ solution essentially corresponds to an eigenvector which is the sum of one x–roll and one y–roll, each one of them changing the direction of rotation at the two central orthogonal vertical planes of the cavity (see Figure 6(c)). Figure 3(a) shows that $S5$ is unstable when it originates at $Ra \simeq 5,902$ and the stability analysis indicates that it has a positive double eigenvalue. This positive double eigenvalue becomes negative at $Ra \simeq 8,300$ and, thus, $S5$ becomes stable at this condition and remains so thereafter.

At the last primary bifurcation identified at $Ra \simeq 7458$ the unstable flow pattern $S4$ sets in. The $S4$ solution has a toroidal configuration and was previously reported by Hernandez and Frederick[17] and by Pallares et al.[15] At slightly supercritical Rayleigh numbers, the $S4$ solution is essentially the sum of two x–rolls and two y–rolls with no change of rotation along their axes (see Figure 6(d)). The flow pattern $S4$ was experimentally identified by Pallares et al.[22] as a transitional state during the start–up of the experimental apparatus, that led to $S1$.

2. Evolution of the stable flow patterns

The simplified descriptions of the $S1$, $S2$, $S5$ and $S4$ patterns given above only hold for Rayleigh numbers slightly above the bifurcation point, where the flow pattern is very similar to the solution of the linearized problem, i.e., very similar to the eigenvector associated with the zero eigenvalue of the Jacobian at the bifurcation point. Note that, as discussed above, the $S1$, $S2$, $S5$ and $S4$ patterns do not possess the antisymmetry properties of the solutions of the linearized problem around the conductive state, which are respectively denoted as $S1_L$, $S2_L$, $S5_L$ and $S4_L$ in Table IV. It is therefore interesting to analyze, at least for the two stable solutions $S1$ and $S5$, how the flow patterns evolve as the Rayleigh number increases.

Figure 7(a) shows the variation with Ra of the cosine of the angle between the solution of the nonlinear problem and the eigenvector associated with the leading eigenvalue predicted by equations linearized around the conductive state for flow patterns $S1$ and $S5$. The results displayed in this figure stress the idea that the Stuart shape assumption[33] holds only for slightly supercritical values of Ra in the current flow system. Moreover, the variation with Ra of the cosine of the angle between the solution of the nonlinear problem and the corresponding solution at the bifurcation Rayleigh number where it sets in is depicted in Figure 7(b) for the single roll ($S1$) and the four rolls ($S5$). These two plots suggest that the spatial structure of both the $S1$ and $S5$ solutions changes significantly with Ra.

Figure 8(a) shows contours of the velocity component normal to the vertical plane $x = 0.25$, together with the projected velocity vectors for a slightly supercritical $S1$ solution at $Ra = 3,500$. The projection of the main roll into this plane is almost perfectly circular with contours at the four corners revealing a significant departure from the antisymmetry properties of the solution of the linearized problem (see Table IV). The corresponding plot for the $S1$ solution at $Ra = 5.0 \times 10^4$ is presented in Figure 8(b). This figure shows that $S1$, while still remaining basically a x-roll flow pattern, has the tendency to elongate in the $y = z$ direction. This elongation explains why the second symmetry matrix for $S1$ in Table III defines a π rotation about the x axis. Moreover, as Ra increases the secondary circulations near the edges of the cavity, although still weak in absolute terms, become increasingly stronger. These secondary vortices are visualized in the projection into the vertical plane $y = 0$ shown in Figure 8(c). Three-dimensional surface plots, not shown here, reveal that the secondary rolls near the four corners are the projection of two vortical structures which are basically parallel to the four edges of the left and right cavity walls, respectively.

On the other hand, Pallares et al.[15] pictured the $S5$ flow motion at $Ra = 10,000$ as a four-roll structure with each roll parallel and close to one of the vertical walls. In the current study it is found that the $S5$ flow pattern becomes much more complex as the Rayleigh number increases. The isosurfaces of $\left\|\vec{V}\right\| = 0.18$ shown in Figure 9(a) suggests that the $S5$ pattern actually consists of two closely interleaved, diagonally aligned vortical structures. This assumption is confirmed by the corresponding plot of selected vortexlines shown in Figure 9(b). Note that the vortexlines have been computed only for the structure with upwelling along two diagonally opposing vertical edges. The global flow picture can be understood as follows. Air flow raising along the two opposing vertical edges reaches the top wall region where it spreads in all directions. A significant part of this flow of spreading air reaches the central region near the top wall before sinking. This in turn results in an important downwelling motion in the central region, as reflected in Figure 9(c) where the projection of the flow into the diagonal plane $x = y$ is shown. The two secondary counter-rotating rolls pictured in the upper half of Figure 9(c) denote a local vorticity alignment normal to this plane. Such a vorticity alignment cannot be observed in Figure 9(b) but would be evident if vortexlines of the second, complementary vortical structure were plotted. Thus the cavity is filled by two big and distinct vortical structures that are however closely interconnected in terms of the resulting flow motion. It is also worth to mention that while vortexlines form closed paths in Figure 9(a) the corresponding flow streamlines, not presented here, do not. Thus, for the problem under study vortexlines seem more appropriate to visualize the flow structure than streamlines.

C. Bifurcations from the convective flow patterns

Figure 3(b) shows that when the $S5$ solution becomes stable at $Ra \simeq 8,300$, two additional unstable flow patterns denoted as $S11$ and $S12$ are developed at this bifurcation point. Table III shows that both solutions have lost two of the symmetries of the $S5$ pattern. At $Ra \simeq 18,826$ the $S11$ solution presents a subcritical steady bifurcation where a new unstable solution, labelled $S13$, sets in. This new solution has lost all the symmetry properties. The $S13$ flow pattern has a saddle-node bifurcation at $Ra \simeq 16,213$ and ends at a new subcritical steady bifurcation of the $S11$ solution that takes place at $Ra \simeq 66,393$. Thus the $S13$ solution connects two steady subcritical bifurcations of $S11$. The $S12$ flow pattern has two steady bifurcations at $Ra \simeq 14,672$ and $Ra \simeq 42,144$ where two new unstable flow patterns labelled $S14$ and $S15$, respectively, set in. Furthermore, the $S12$ solution presents a pair of saddle-node bifurcations at $Ra \simeq 56,528$ and $Ra \simeq 36,654$. The $S15$ solution has also a pair of saddle-node bifurcations at $Ra \simeq 45,650$ and $Ra \simeq 45,363$. All flow patterns S_i, $i = 11, \cdots, 15$ are less efficient than $S5$ in transferring heat and remain unstable for values of Ra up to 1.5×10^5.

Figure 3(a) shows that the $S1$ solution is stable when it sets in and remains stable until a further bifurcation takes place at $Ra \simeq 66,153$. At this bifurcation point $S1$ becomes unstable and a new stable flow pattern named $S7$ develops. This transition from $S1$ to $S7$ is consistent with the one observed in the experiments by Pallares et al.[22] at $Pr = 130$. Figures 10(a) and (b) present contours and vectors plots at the planes $x = 0.25$ and $y = 0$, respectively, for the $S7$ solution at $Ra = 10^5$. Figure 10(a) shows the breaking of symmetry for the $S7$ flow pattern when compared to the corresponding $S1$ pattern in Figure 8(b). Table III shows that the symmetry which is lost is the rotation of angle π around the x-axis.

From the mathematical point of view, it is observed that while the solution $S1$ only presents symmetry blocks 4 and 7 (see Table I for the symmetry classes of velocity and temperature associated with each block), the $S7$ solution also presents blocks 3 and 8. This mathematical interpretation is relevant because it can be shown that the $S7$ solution consists of the superposition of a pattern with only symmetry blocks 3 and 8 to the basic $S1$ pattern, which is formed by symmetry blocks 4 and 7. The presence of such a superposed pattern is reflected in the pair of counter-rotating rolls near the bottom boundary and the vertical midline in Figure 10(b). The secondary rolls that are characteristic of the $S1$ pattern in Figure 8(c) are also present in the $S7$ solution portrayed in Figure 10(b), although the ones at the bottom corners are hardly visible.

The three-dimensional structure of these secondary vortices is better portrayed with the help of a scalar quantity called helicity (the dot product of velocity and vorticity), H. Figure 10(c) presents isosurfaces of $H = 0.083$ for the same $S7$ solution at $Ra = 10^5$. This plot shows that, as was the case for the $S1$ pattern, the four corner rolls in Figure 10(b) are projections of two large secondary vortical structures, each one close and parallel to one lateral wall. These two secondary vortices follow the curved boundary of the main roll and, because of the loss of symmetry of the $S7$ pattern, are much stronger along the top and rear walls. Note that the pair of central rolls at the bottom of Figure 10(b) actually denote two independent vortical structures in the helicity plot of Figure 10(c). This pair of vortices span the bottom cavity wall and also follow the curved boundary of the main roll. In fact, they resemble the Görtler-like secondary vortices that appear in lid-driven cavity flows.[34,35] It may therefore be argued that the bifurcation where the $S7$ flow pattern emanates is the result of a centrifugal instability of the main x–roll.

The other two stable solutions in the bifurcation diagram of Figure 3(a) are the ones labelled as $S8$ and $S10$. This isolated solution branch which was not identified by the continuation method, was initialized from the projection of a discrete field, calculated by a fourth-order finite difference solver at $Ra = 80,000$, and traced thereafter by the continuation method. The initially stable $S8$ and the unstable $S9$ solutions set in at $Ra \simeq 76,770$ as a result of a saddle-node bifurcation. Figures 11(a1) and 11(a2) show the vertical velocity contours in the horizontal midplane $z = 0$ for the $S8$ flow pattern at $Ra = 80,000$. There is a good agreement between the isocontours predicted by the fourth-order finite difference solver and by the Galerkin method. Table V shows that a good quantitative agreement is obtained for all the steady stable flow patterns identified by the present work. The $S8$ structure consists of two asymmetric counter-rotating rolls aligned along one of the $x = \pm y$ diagonals. Note that $S8$ has a certain similarity to the $S2$ pattern presented in Figure 6(b). In Table III, the first symmetry matrix for $S2$ and the symmetry matrix for $S8$ do not coincide because of the different diagonal orientation chosen by the particular realizations of Figures 6(b) and 11(a). The real difference between these two patterns is the presence of the second smaller roll in the $S8$ pattern of Figures 11(a). The $S8$ solution is only stable up to $Ra \simeq 86,507$ where a symmetry-breaking bifurcation occurs into the initially stable $S10$ pattern portrayed in Figures 11(b1) and 11(b2). At $Ra = 87,000$, departure from diagonal symmetry of the $S10$ solution is hardly visible in Figure 11(b1). As the Rayleigh number is increased, it becomes more evident that the $S10$ has no symmetry element, as shown in the contours for $Ra = 1.2 \times 10^5$ in Figure 11(b2). Note that at this Rayleigh number the $S10$ solution is already unstable as a consequence of the Hopf bifurcation occurring at $Ra \simeq 94,800$.

D. Heat transfer

It is interesting to note that the most efficient flow pattern in transferring heat is $S4$ (see Figure 3(a)), which is unstable over the whole range of Ra investigated. This instance seems to contradict the so called Malkus principle,[36] or, rather, Malkus conjecture, which postulates that flows that maximize convective heat transfer should be realized and/or prevalent. A different way of analyzing the information in Figure 3(a) is shown in Figure 12 where the $\log\left(\frac{Nu-Nu_0}{Nu_0}\right)$ is depicted as a function of $\log\left(\frac{Ra-Ra_0}{Ra_0}\right)$ for most of the flow patterns shown in Figure 3(a). Here Ra_0 represents the value of the bifurcation Rayleigh number where a solution sets in and Nu_0 the corresponding value of the Nusselt number. Note that while the unstable $S4$ flow pattern has the highest slope the $S5$ flow pattern is the one crossing the ordinate axis at the highest location.

It is also relevant in Figure 12 that the slope for the $S7$ flow pattern is almost as high as those values correspondig to solutions that set in at primary bifurcations. This means that the flow pattern $S7$ (see Figures 10) that emanates from the $S1$ branch is able to considerably increase the rate of heat transfer. At the point of the $S1$–$S7$ bifurcation in Figure 3(a) the slope of the $S1$ branch has become small and this pattern is relatively inefficient to transfer heat. The enhanced heat transfer ability of the $S7$ pattern is to be attributted to the presence of the Görtler-like vortices visualized in Figures 10(b) and (c).

The distributions of the local Nusselt number on the bottom wall are shown in Figures 13(a) and (b) for the $S1$ and $S7$ patterns, respectively. Figure 13(a) shows that the maximum heat transfer in the $S1$ pattern occurs at two lobes corresponding to the maximum impingement of the x–roll motion on the bottom wall. The only significant difference in Figure 13(b) for the $S7$ pattern is the increased height of the two maxima. Figure 10(b) reflects that in the region in between the pair of Görtler-like vortices near the bottom wall there is little y-motion. The corresponding plot of isotherms, not included here, shows that the region with deficit in y-motion has also a very low temperature departure, i.e., $\theta \approx 0$. The pair of secondary Görtler-like vortices thus favours mixing between cold and warm air. It is also benefitial, in terms of heat transfer in the $S7$ pattern, that air moving near the bottom wall centerline follows helicoidal paths. The average time of residence of air near the bottom wall in $S7$ is thus higher than it is in the $S1$ pattern, where air basically follows straight paths.

As shown in Figure 12, the $S5$ solution has a slower decay on the relative ability to transfer heat than have the $S1$ and $S2$ patterns. The local Nusselt distribution in Figure 13(c) shows that most of the heat in $S5$ is transferred in the corner regions where the impingement of downwelling cold air occurs. Notwithstanding, as discussed in Section IVB, the flow structure $S5$ is significantly modified as Ra increases. Here lies, probably, its relative advantage with respect to the $S1$ pattern whose secondary motions are constrained to the edges of the cavity and thus remain relatively irrelevant in terms of heat transfer. Figure 9(c) shows that motion in the central region of the cavity for $S5$ at $Ra = 1.5 \times 10^5$ has become quite significant. Although the secondary rolls portrayed in Figure 9(c) produce no net transport of air between the top and bottom halves of the cavity, they contribute to the overall transfer of heat by recirculating not sufficiently cool air into the top wall. From the heat transport standpoint, secondary motion in the $S5$ solution plays the same role as do recycle streams in a chemical plant, i.e., they increase the overall conversion between hot and cold air (or viceversa) at the top/bottom walls.

V. Concluding remarks

The study of bifurcations and stability of the steady convective flow of air in a cubical enclosure heated from below has been carried out using a Galerkin spectral method and parameter continuation techniques. Present results reveal that different stable steady flow patterns can coexist for moderate values of Ra, the final asymptotic state depending on initial conditions. At the first primary bifurcation ($Ra_c = 3,389$) an x–roll $S1$ and a diagonal–roll (x–roll $\pm$ y–roll) $S2$ are formed. While the latter is unstable over the whole range of Ra studied ($Ra < 1.5 \times 10^5$) the former is stable when it appears but becomes unstable at $Ra \simeq 66,153$. At this bifurcation point a stable $S7$ flow pattern sets in and remains stable up to $Ra = 1.5 \times 10^5$. The second primary bifurcation at $Ra \simeq 5,902$ yields an initially unstable four–roll structure $S5$ that stabilizes at $Ra \simeq 8,300$. The additional flow structures that appear at this secondary bifurcation turn out to be unstable over the whole range of Ra considered.

Furthermore, two flow patterns, denoted as $S8$ and $S9$, for which no connection has been found with any branch bifurcated from the conductive state, have been identified. From the stability analysis it is concluded that these solutions set in as a consequence of a saddle-node bifurcation. While the $S8$ solution is stable for a narrow range of Ra ($76,770 \leq Ra \leq 86,057$), the $S9$ solution remains unstable over the whole range of Ra studied. When $S8$ becomes unstable at $Ra \simeq 86,057$ a new flow pattern $S10$ originates which is stable up to $Ra \simeq 94,800$ where it becomes unstable as a consequence of a Hopf bifurcation.

On the other hand, it is worth to note that the solutions of the nonlinear problem and the solutions of the problem linearized around the conductive state are different not only in the detail but even in regard to their intrinsic symmetries. Not surprisingly, while solutions of the nonlinear problem present only symmetry groups, solutions of the problem linearized around a steady solution possess both symmetry and antisymmetry groups. At slightly supercritical Rayleigh numbers, solutions of the nonlinear problem seem to possess all of the symmetry properties of solutions of the problem linearized around the corresponding steady solutions. However, as the Rayleigh number is increased, differences between solutions of the linear and nonlinear problem become evident. This stresses the idea that the Stuart shape assumption can only be accepted with a local character in Ra. Moreover, in the $S1$–$S7$ and $S8$–$S10$ transitions between stable structures it is observed that the bifurcated solution has lost one of the symmetries present in the parent structure.

The bifurcation diagram calculated in the present study presents important discrepancies with previous numerical studies. The only flow patterns found by Pallares et al.[22] in visualization and PIV experiments at $Pr = 130$ are the flow patterns $S1$ $S2$ and $S7$. The four-roll flow pattern $S5$ was characterized experimentally[22] only when perfectly conducting side walls were used and the flow pattern $S4$ was identified just as a transitional state. Furthermore, the current work predicts a transition between $S1$ and $S7$ which was also observed experimentally[22] but was not properly described by previous numerical calculations. Thus, the present study clarifies incompleteness of previous calculations and provides a better description of experimental results published in the literature.

Complementary fourth-order finite difference calculations are found to properly characterize all of the stable flow structures within the consistent ranges of Ra. Morever, the time-marching calculations have been useful in locating the $S8$ solution branch, which would most probably have been missed otherwise by the continuation method. The cause that numerically predicted stable flow patterns, such as $S8$, have not been observed experimentally could be the fact that the basin of attraction of that flow pattern would not overlap with the initial conditions accessible to the experiment. In addition, the time-marching code yields a stable time-periodic structure of the single-roll type for $Ra \geq 1.2 \times 10^5$. Future research will be oriented to further develop the present algorithm in order to continue those solutions branchs that are originated in the Hopf bifurcation point ($Ra \geq 94,800$). This will broad the bifurcation diagram up to much higher values of the Rayleigh number.

Acknowledgments

The authors D. P., J. H. and F. G. are grateful for the financial support received from DGICYT projects PPQ2000-1339 and PPQ2001-1519 and from the CIRIT "Programa de Grups de Recerca Consolidats de la Generalitat de Catalunya", projects 1998SGR-00102, 2000SGR-00103 and 2001SGR-00324. The research of C. S. has been supported by DGICYT projects BFM2000-805 and BFM2003-09504-C02-01 (Spain) and grant CIRIT 2001SGR-70 (Catalonia).

Appendix.

The matrix L in equations (20) and (21) is block-diagonal with eigth different blocks, each block corresponding to a subspace generated by one of the eight classes described in (18). Each one of these blocks has the structure

$$\begin{pmatrix} M_1 & Ra^{\frac{1}{2}} M_2^T \\ Ra^{\frac{1}{2}} M_2 & M_1 \end{pmatrix}. \tag{A1}$$

In expression (A1) M_1 and M_2 are defined as

$$\begin{aligned} M_1(j,i) &= \langle \nabla^2 \vec{F}_i,\, \vec{F}_j \rangle, \\ M_2(j,i) &= \langle F_i^{(4)},\, F_j^{(3)} \rangle. \end{aligned} \tag{A2}$$

Matrices B and Q are defined as

$$B(j,i) = \langle \begin{pmatrix} \frac{1}{Pr} F_i^{(1)} \\ \frac{1}{Pr} F_i^{(2)} \\ \frac{1}{Pr} F_i^{(3)} \\ F_i^{(4)} \end{pmatrix}, \begin{pmatrix} F_j^{(1)} \\ F_j^{(2)} \\ F_j^{(3)} \\ F_j^{(4)} \end{pmatrix} \rangle, \quad Q(j,i,n) = \langle \begin{pmatrix} \frac{1}{Pr} \sum_{r=1}^{3} F_i^{(r)} D_r F_n^{(1)} \\ \frac{1}{Pr} \sum_{r=1}^{3} F_i^{(r)} D_r F_n^{(2)} \\ \frac{1}{Pr} \sum_{r=1}^{3} F_i^{(r)} D_r F_n^{(3)} \\ \sum_{r=1}^{3} F_i^{(r)} D_r F_n^{(4)} \end{pmatrix}, \begin{pmatrix} F_j^{(1)} \\ F_j^{(2)} \\ F_j^{(3)} \\ F_j^{(4)} \end{pmatrix} \rangle. \tag{A3}$$

In expressions (A2) and (A3) $\vec{F}_j$ is the normalized jth-basis function used to expand $\begin{pmatrix} \vec{V} \\ \theta \end{pmatrix}$ according to equation (19), the superscript (k) refers to the kth-component of the basis function $\vec{F}$ and the angles $\langle\ ,\ \rangle$ denote the internal product.

References

[1]E. Bodenschatz, W. Pesch, and G. Ahlers, Annu. Rev. Fluid Mech. **32**, 709 (2000).

[2]A. V. Getling, *Rayleigh-Bénard convection: structures and dynamics*, volume 11 of *Advanced Series in Nonlinear Dynamics*, World Scientific Publishing, 1998.

[3]E. L. Koschmieder, *Bénard Cells and Taylor Vortices*, Cambridge Monographs on Mechanics and Applied Mathematics, Cambridge University Press, Cambridge, 1993.

[4]G. D. V. Davis, Int. J. Numer. Meth. Fluids **3**, 249 (1983).

[5]A. Y. Gelfgat, J. Comput. Physics **156**, 300 (1999).

[6]H. A. Dijkstra, Test problem: Rayleigh–Bénard convection, 1988, Internet address: http://www.euromech.cz/Text/finalr98.phtml.

[7]F. H. Busse and R. M. Clever, J. Fluid Mech. **91**, 319 (1979).

[8]R. M. Clever and F. H. Busse, J. Fluid Mech. **65**, 625 (1974).

[9]F. H. Busse, Rep. Prog. Phys. **41**, 1929 (1978).

[10]I. Catton, Transactions of the ASME **110**, 1154 (1988).

[11]R. W. M. Henkes and P. L. Quéré, J. Fluid Mech. **319**, 281 (1996).

[12]A. Schlüter, D. Lortz, and F. H. Busse, J. Fluid Mech. **23**, 129 (1965).

[13]R. Kessler, J. Fluid Mech. **174**, 357 (1987).

[14]J. A. C. Humphrey, J. Cushner, M. Al-Shannag, J. Herrero, and F. Giralt, ASME J. Fluids Engineering **125**, 130 (2003).

[15]J. Pallarès, F. X. Grau, and F. Giralt, Int. J. Heat Mass Transfer **42**, 753 (1999).

[16]R. J. A. Janssen and R. A. W. M. Henkes, Phys. Fluids **8**, 62 (1996).

[17]R. Hernández and R. Frederick, Int. J. Heat Mass Transfer **37**, 411 (1994).

[18]A. Y. Gelfgat, P. Z. Bar-Yoseph, and A. L. Yarim, J. Fluid Mech. **388**, 315 (1999).

[19]K. H. Winters, K. A. Cliffe, and C. P. Jackson, in *Numerical Methods for Transient and Coupled Problems*, edited by R. W. Lewis, E. Hinton, P. Bettess, and B. A. Schrefler, John Wiley & Sons, 1987, pp. 179–198.

[20]P. C. Dauby and G. Lebon, J. Fluid Mech. **329**, 25 (1996).

[21]S. H. Davis, J. Fluid Mech. **465**, 30 (1967).

[22]J. Pallarès, M. Arroyo, F. X. Grau, and F. Giralt, Experiments in Fluids **31**, 208 (2001).

[23]I. Catton, Int. J. Heat Mass Transfer **15**, 665 (1972).

[24]C. Canuto, M. Y. Hussaini, and A. Quarteroni, *Spectral Methods in Fluid Dynamics*, Springer Series in Computational Physics, Springer Verlag, New York, 1987.

[25]F. Marquès, Phys. Fluids **2**, 729 (1990).

[26]Cray User Group Spring Proceedings, *Bifurcations from the conductive state in a cubical cavity heated from below*, 1996.

[27]L. Harris and W. H. Reid, ASME J. Heat Transfer **93**, 188 (1959).

[28]K. H. Winters, Computer Physics Communications **65**, 299 (1991).

[29]R. Seydel, *Practical Bifurcations and Stability Analysis: from Equilibrium to Chaos*, Springer-Verlag, New York, second edition, 1994.

[30]C. Simó, in *Modern methods in celestial mechanics*, edited by D. Benest and C. Froeschlé, Editions Frontières, Paris, 1990, pp. 285–330.

[31]R. B. Lehoucq and D. C. Sorensen, SIAM J. Matrix Anal. Appl. **17**, 789 (1996).

[32]H. Ozoe, K. Yamamoto, S. W. Churchill, and H. Sayama, ASME J. Heat Transfer **98**, 202 (1976).

[33]J. T. Stuart, J. Fluid Mech. **4**, 1 (1958).

[34]Y. D. Spasov, J. Herrero, F. X. Grau, and F. Giralt, Phys. Fluids **15**, 134 (2003).

[35]S. Albensoder, H. Kuhlmann, and H. Rath, Phys. Fluids **13**, 121 (2001).

[36]W. V. R. Malkus and G. Veronis, J. Fluid Mech. **4**, 225 (1958).

	Block 1	Block 2	Block 3	Block 4	Block 5	Block 6	Block 7	Block 8
u	EEO	EOO	OEO	OOO	EEE	EOE	OEE	OOE
v	EEO	EOO	OEO	OOO	EEE	EOE	OEE	OOE
w	OEE	OOO	EEE	EOE	OEO	OOO	EEO	EOO
θ	OEE	OOO	EEE	EOE	OEO	OOO	EEO	EOO

Table I. Symmetry classes of temperature and velocity associated with each block.

Flow pattern	$N_{xyz} = 5$	$N_{xyz} = 6$	$N_{xyz} = 7$	$N_{xyz} = 8$	$\Delta_{8-7}\%$
x–roll ($S1$)	3391.17	3390.09	3389.53	3389.21	0.0094
four–rolls ($S5$)	5910.09	5906.03	5903.97	5902.81	0.0197
$2x$–rolls + $2y$–rolls ($S4$)	7462.98	7459.79	7458.35	7457.59	0.0102

Table II. Convergence of the Rayleigh number at which bifurcation from the conductive state occurs as a function of the truncation parameters $N_{xyz} = N_x = N_y = N_z$ used. The last column includes the relative differences between $N_{xyz} = 8$ and $N_{xyz} = 7$.

Flow Pattern	Blocks	Generators of the Symmetry Group	Range of Stability	Range of Instability
$S1$	4, 7	$\begin{pmatrix} -1 & 0 & 0 \\ 0 & 1 & 0 \\ 0 & 0 & 1 \end{pmatrix} \begin{pmatrix} 1 & 0 & 0 \\ 0 & -1 & 0 \\ 0 & 0 & -1 \end{pmatrix}$	3389 – 66153	66153–
$S2$	1, 4, 6, 7	$\begin{pmatrix} 0 & -1 & 0 \\ -1 & 0 & 0 \\ 0 & 0 & 1 \end{pmatrix} \begin{pmatrix} 0 & 1 & 0 \\ 1 & 0 & 0 \\ 0 & 0 & -1 \end{pmatrix}$	–	3389–
$S4$	3, 7	$\begin{pmatrix} -1 & 0 & 0 \\ 0 & 1 & 0 \\ 0 & 0 & 1 \end{pmatrix} \begin{pmatrix} 1 & 0 & 0 \\ 0 & -1 & 0 \\ 0 & 0 & 1 \end{pmatrix}$ $\begin{pmatrix} 0 & 1 & 0 \\ 1 & 0 & 0 \\ 0 & 0 & 1 \end{pmatrix} \begin{pmatrix} 0 & -1 & 0 \\ -1 & 0 & 0 \\ 0 & 0 & 1 \end{pmatrix}$	–	7457–
$S5$	2, 7	$\begin{pmatrix} -1 & 0 & 0 \\ 0 & 1 & 0 \\ 0 & 0 & -1 \end{pmatrix} \begin{pmatrix} 0 & 1 & 0 \\ 1 & 0 & 0 \\ 0 & 0 & 1 \end{pmatrix} \begin{pmatrix} 0 & -1 & 0 \\ -1 & 0 & 0 \\ 0 & 0 & 1 \end{pmatrix}$	8300–	5903 – 8300
$S6$	3, 7	$\begin{pmatrix} -1 & 0 & 0 \\ 0 & 1 & 0 \\ 0 & 0 & 1 \end{pmatrix} \begin{pmatrix} 1 & 0 & 0 \\ 0 & -1 & 0 \\ 0 & 0 & 1 \end{pmatrix}$	–	10034–
$S7$	3, 4, 7, 8	$\begin{pmatrix} -1 & 0 & 0 \\ 0 & 1 & 0 \\ 0 & 0 & 1 \end{pmatrix}$	66153–	–
$S8$	All	$\begin{pmatrix} 0 & 1 & 0 \\ 1 & 0 & 0 \\ 0 & 0 & 1 \end{pmatrix}$	76775 – 86507	86507–
$S9$	All	$\begin{pmatrix} 0 & 1 & 0 \\ 1 & 0 & 0 \\ 0 & 0 & 1 \end{pmatrix}$	–	76775–
$S10$	All	–	86507 – 94800	94800–
$S11$	All	$\begin{pmatrix} 0 & -1 & 0 \\ -1 & 0 & 0 \\ 0 & 0 & 1 \end{pmatrix}$	–	8300–
$S12$	2,7,1,8	$\begin{pmatrix} -1 & 0 & 0 \\ 0 & 1 & 0 \\ 0 & 0 & -1 \end{pmatrix}$	–	8300–
$S13$	All	–	–	18826 – 66393
$S14$	All	–	–	14672–
$S15$	All	–	–	42144–

Table III. Summary of the main features of all solutions identified in the nonlinear problem.

Flow Pattern	**Blocks**	**Generators of the Symmetry Group**	**Generators of the Antisymmetry Group**
$S1_L$	4	$\begin{pmatrix} -1 & 0 & 0 \\ 0 & 1 & 0 \\ 0 & 0 & 1 \end{pmatrix} \begin{pmatrix} 1 & 0 & 0 \\ 0 & -1 & 0 \\ 0 & 0 & -1 \end{pmatrix}$	$\begin{pmatrix} 1 & 0 & 0 \\ 0 & -1 & 0 \\ 0 & 0 & 1 \end{pmatrix} \begin{pmatrix} 1 & 0 & 0 \\ 0 & 1 & 0 \\ 0 & 0 & -1 \end{pmatrix}$
$S2_L$	1, 4	$\begin{pmatrix} 0 & -1 & 0 \\ -1 & 0 & 0 \\ 0 & 0 & 1 \end{pmatrix} \begin{pmatrix} 0 & 1 & 0 \\ 1 & 0 & 0 \\ 0 & 0 & -1 \end{pmatrix}$	$\begin{pmatrix} 1 & 0 & 0 \\ 0 & 1 & 0 \\ 0 & 0 & -1 \end{pmatrix} \begin{pmatrix} 0 & 1 & 0 \\ 1 & 0 & 0 \\ 0 & 0 & 1 \end{pmatrix}$
$S4_L$	3	$\begin{pmatrix} -1 & 0 & 0 \\ 0 & 1 & 0 \\ 0 & 0 & 1 \end{pmatrix} \begin{pmatrix} 1 & 0 & 0 \\ 0 & -1 & 0 \\ 0 & 0 & 1 \end{pmatrix}$ $\begin{pmatrix} 0 & 1 & 0 \\ 1 & 0 & 0 \\ 0 & 0 & 1 \end{pmatrix} \begin{pmatrix} 0 & -1 & 0 \\ -1 & 0 & 0 \\ 0 & 0 & 1 \end{pmatrix}$	$\begin{pmatrix} 1 & 0 & 0 \\ 0 & 1 & 0 \\ 0 & 0 & -1 \end{pmatrix}$
$S5_L$	2	$\begin{pmatrix} -1 & 0 & 0 \\ 0 & 1 & 0 \\ 0 & 0 & -1 \end{pmatrix} \begin{pmatrix} 0 & 1 & 0 \\ 1 & 0 & 0 \\ 0 & 0 & 1 \end{pmatrix}$ $\begin{pmatrix} 0 & -1 & 0 \\ -1 & 0 & 0 \\ 0 & 0 & 1 \end{pmatrix}$	$\begin{pmatrix} -1 & 0 & 0 \\ 0 & 1 & 0 \\ 0 & 0 & 1 \end{pmatrix} \begin{pmatrix} 1 & 0 & 0 \\ 0 & -1 & 0 \\ 0 & 0 & 1 \end{pmatrix}$ $\begin{pmatrix} 1 & 0 & 0 \\ 0 & 1 & 0 \\ 0 & 0 & -1 \end{pmatrix}$

Table IV. Summary of the main features of the linearized solutions around the motionless conductive state.

Flow pattern	Ra	$\cos\rho_\theta$	$\cos\rho_{\vec{V}}$
$S1$	6.0×10^4	0.99999	0.99998
$S5$	1.5×10^5	0.99996	0.99990
$S7$	1.5×10^5	0.99990	0.99994
$S8$	8.0×10^4	0.99987	0.99966
$S10$	9.0×10^4	0.99975	0.99933

Table V. Cosines of the angles ρ_θ and $\rho_{\vec{V}}$ for stable flow patterns near the highest Ra where they are stable. ρ_θ is the angle between the temperature field over a $41\times41\times41$ uniform mesh obtained from the results of the Galerkin continuation method and the time-marching method, respectively; $\rho_{\vec{V}}$ is defined analogously for the velocity field.

Figure Captions

Figure 1. Logarithm of the absolute value of the spectral coefficients of the x–roll flow pattern developed at $Ra = 1.5 \times 10^5$ for the truncation parameters $N_{xyz} = N_x = N_y = N_z = 7$. Only spectral coefficients associated with basis functions used to expand temperature are plotted. The abscissa is the global spherical frequency $ns = \sqrt{(i^2 + j^2 + k^2)}$. The least squares line which has a slope value equal to -0.555 is also plotted. The linear correlation coefficient is equal to -0.87

Figure 2. Effect on the results of the basis used in the calculations. (a) Variation of the Nusselt number (Nu) with respect to the Rayleigh number (Ra) for the x–roll flow pattern. The solid line denotes the calculation with the complete basis and $N_{xyz} = N_x = N_y = N_z = 7$ as in Figure 1. The result shown with dashed line has been obtained with an incomplete basis not including the subset $\vec{G}^{(3)}_{ijk}$ in equation (17). In both cases the filled circle denotes the predicted value of the Rayleigh number where the solution becomes unstable. Variation with the Rayleigh number of the leading eigenvalues for the calculations with (b) the full basis, and (c) the incomplete basis. Logarithmic scale is used in the Ra axis.

Figure 3. Bifurcation diagram at $Pr = 0.71$. Stable flow patterns are depicted with solid lines. Unstable flow patterns are represented by dashed lines when they have exactly one unstable eigenmode and by dotted lines when they have two or more unstable eigenmodes. Steady, Hopf and saddle-node bifurcations are represented with filled circles, hollow circles and hollow squares, respectively. (a) The Nusselt number Nu is depicted as a function of Ra. (b) The value $Nu - 0.01Ra^{\frac{1}{2}}$ is depicted as a function of Ra.

Figure 4. The real part of the leading eigenvalue is depicted as a function of $10^{-3}Ra$ for most of the flow patterns identified.

Figure 5. Numerical finite difference results. The Nusselt number Nu is depicted as a function of Ra at $Pr = 0.71$.

Figure 6. Vertical velocity contours in the horizontal midplane $z = 0$ for the flow patterns $S1$, $S2$, $S4$ and $S5$ at values of Ra slightly above the bifurcation points where they set in.

Figure 7. Variation with Ra of the cosine of (a) the angle between the solution of the nonlinear problem and the eigenvector associated with the leading eigenvalue predicted by equations linearized around the motionless conductive state for the single roll ($S1$) and the four rolls ($S5$), (b) the angle between the solution of the nonlinear problem and the corresponding solution at the bifurcation Rayleigh number where it sets in for the single roll ($S1$) and the four rolls ($S5$).

Figure 8. Contours of the velocity component normal to the vertical plane $x = 0.25$, together with the projected velocity vectors for the $S1$ flow pattern (x–roll) at (a) $Ra = 3,500$ and (b) $Ra = 50,000$. (c) The same type of plot for the vertical plane $y = 0$ at $Ra = 50,000$.

Figure 9. $S5$ flow pattern at $Ra = 1.5 \times 10^5$. (a) Isosurfaces of $||\vec{V}|| = 0.18$. (b) Selected vortexlines denoting the shape of the vortical structure with upwelling motion along two vertical edges of the cavity. (c) Vertical velocity contours together with velocity vectors at the vertical diagonal plane $x = y$.

Figure 10. $S7$ flow pattern at $Ra = 10^5$. (a) Contours of the velocity component normal to the plane $x = 0.25$ together with the projected velocity vectors. (b) The same type of plot for the vertical plane $y = 0$. (c) Isosurfaces with helicity value $H = 0.083$.

Figure 11. Vertical velocity contours in the horizontal midplane $z = 0$ for the $S8$ flow pattern at $Ra = 80,000$ obtained (a1) by the finte-difference method and (a2) by the Galerkin method. The same kind of plot for the $S10$ flow pattern obtained by the Galerkin method at (b1) $Ra = 87,000$ and (b2) $Ra = 1.2 \times 10^5$.

Figure 12. Variation of $\log\left(\frac{Nu-Nu_0}{Nu_0}\right)$ as a function of $\log\left(\frac{Ra-Ra_0}{Ra_0}\right)$ for most of the flow patterns identified. Here Ra_0 represents the value of the bifurcation Rayleigh number where a solution sets in and Nu_0 the corresponding value of the Nusselt number.

Figure 13. Distribution of the local Nusselt number at the bottom wall of the cavity for (a) $S1$ pattern at $Ra = 60,000$; (b) $S7$ pattern at $Ra = 10^5$; and, (c) $S5$ pattern at $Ra = 1.5 \times 10^5$.

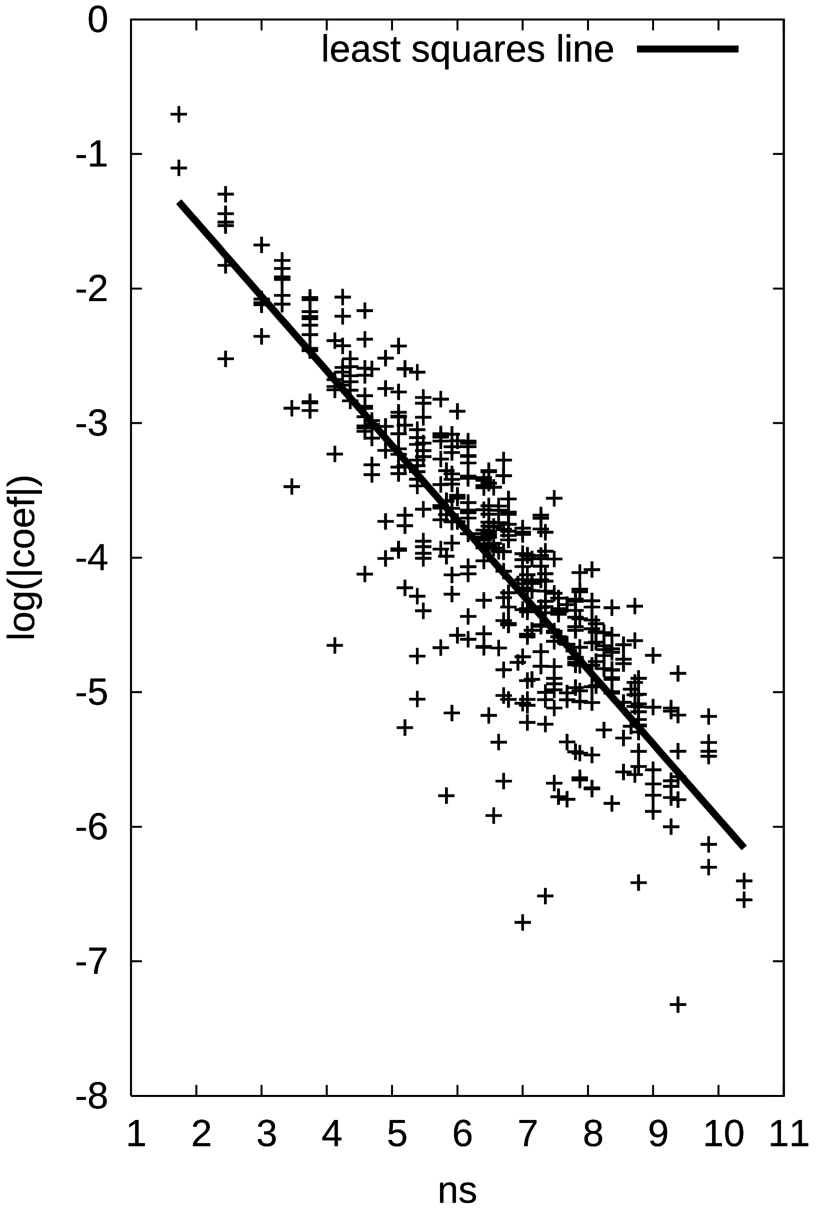

Figure 1: Logarithm of the absolute value of the spectral coefficients of the x–roll flow pattern developed at $Ra = 1.5\times10^5$ for the truncation parameters $N_{xyz} = N_x = N_y = N_z = 7$. Only spectral coefficients associated with basis functions used to expand temperature are plotted. The abscissa is the global spherical frequency $ns = \sqrt{(i^2 + j^2 + k^2)}$. The least squares line which has a slope value equal to -0.555 is also plotted. The linear correlation coefficient is equal to -0.87.

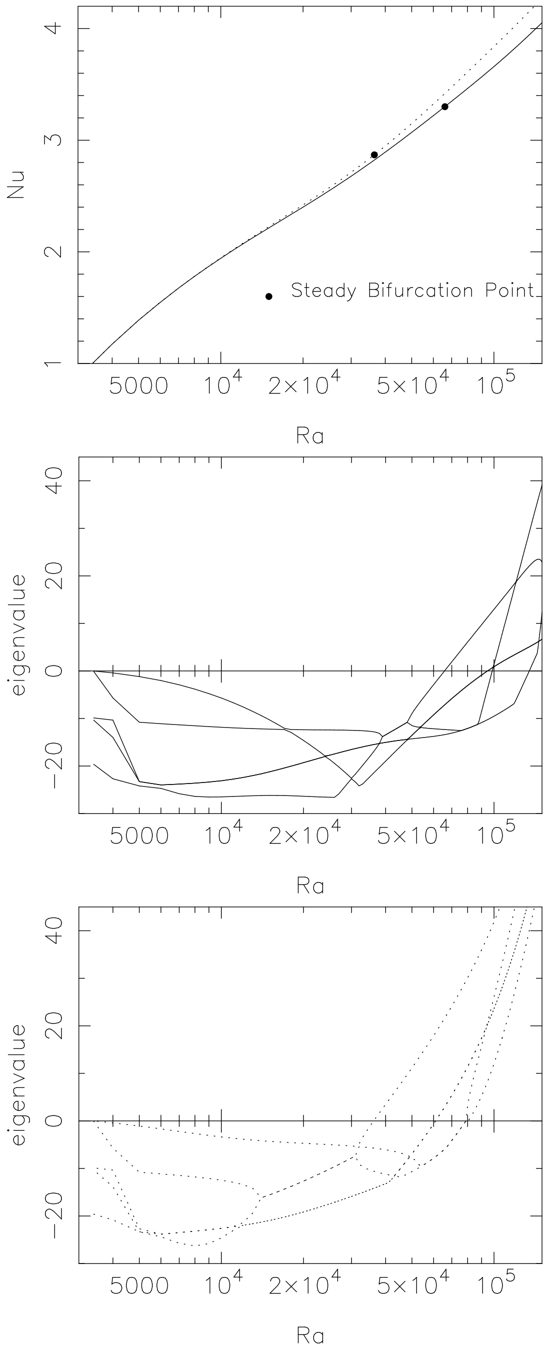

(a)

(b)

(c)

Figure 2: Effect on the results of the basis used in the calculations. (a) Variation of the Nusselt number (Nu) with respect to the Rayleigh number (Ra) for the x–roll flow pattern. The solid line denotes the calculation with the complete basis and $N_{xyz} = N_x = N_y = N_z = 7$ as in Figure 1. The result shown with dashed line has been obtained with an incomplete basis not including the subset $\vec{G}^{(3)}_{ijk}$ in equation (17). In both cases the filled circle denotes the predicted value of the Rayleigh number where the solution becomes unstable. Variation with the Rayleigh number of the leading eigenvalues for the calculations with (b) the full basis, and (c) the incomplete basis. Logarithmic scale is used in the Ra axis.

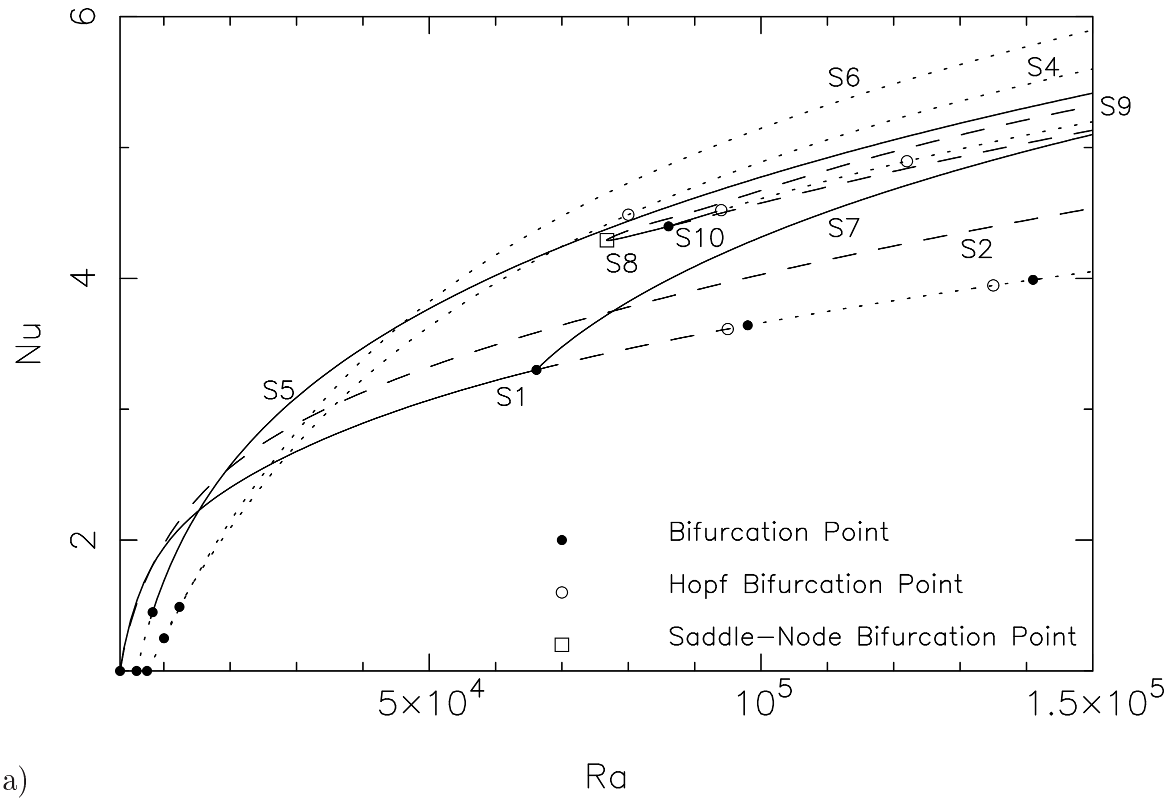

6
4
2
Nu
5×10^4
10^5
1.5×10^5
Ra
S6
S4
S9
S10
S8
S7
S2
S5
S1
Bifurcation Point
Hopf Bifurcation Point
Saddle–Node Bifurcation Point

a)

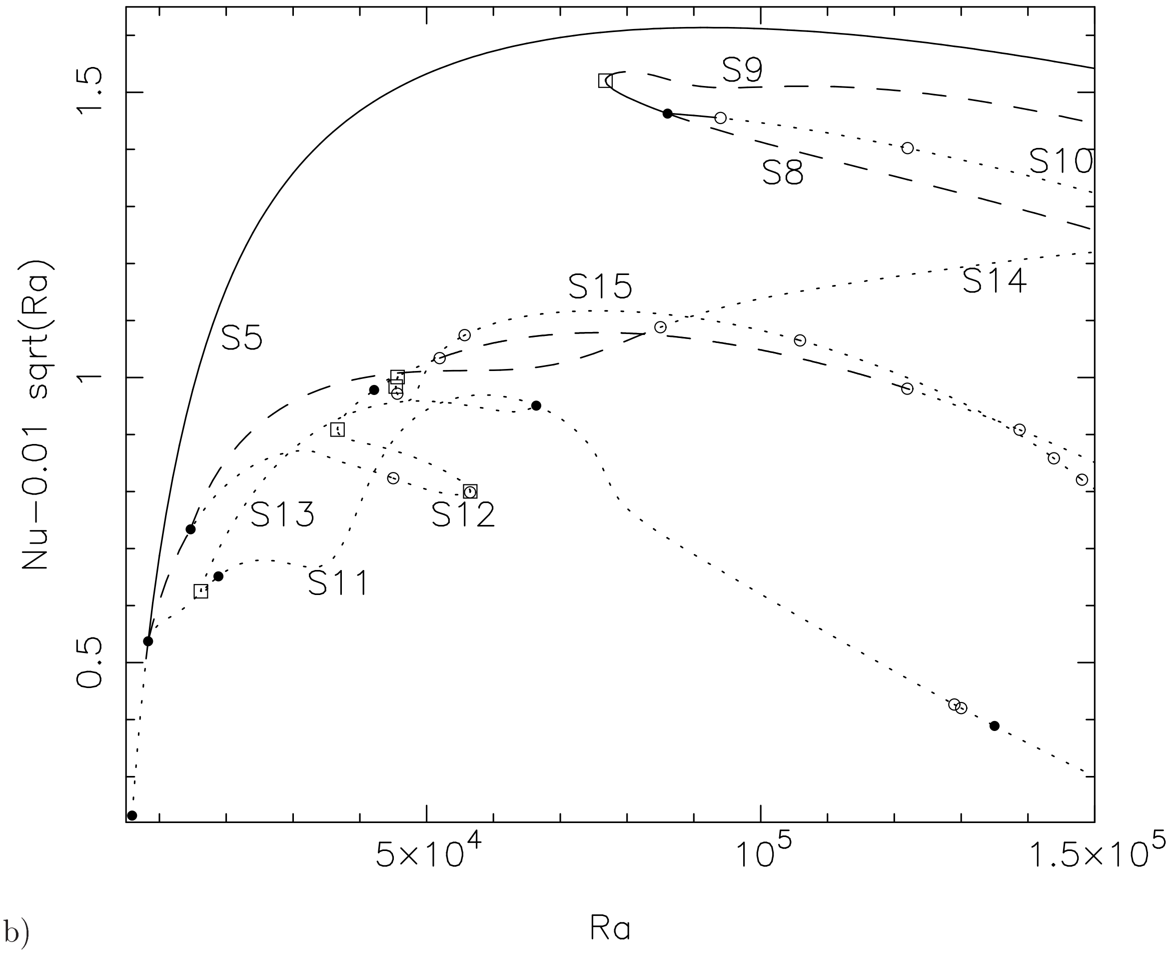

b)

Figure 3: Bifurcation diagram at $Pr = 0.71$. Stable flow patterns are depicted with solid lines. Unstable flow patterns are represented by dashed lines when they have exactly one unstable eigenmode and by dotted lines when they have two or more unstable eigenmodes. Steady, Hopf and saddle-node bifurcations are represented with filled circles, hollow circles and hollow squares, respectively. (a) The Nusselt number Nu is depicted as a function of Ra. (b) The value $Nu - 0.01Ra^{\frac{1}{2}}$ is depicted as a function of Ra.

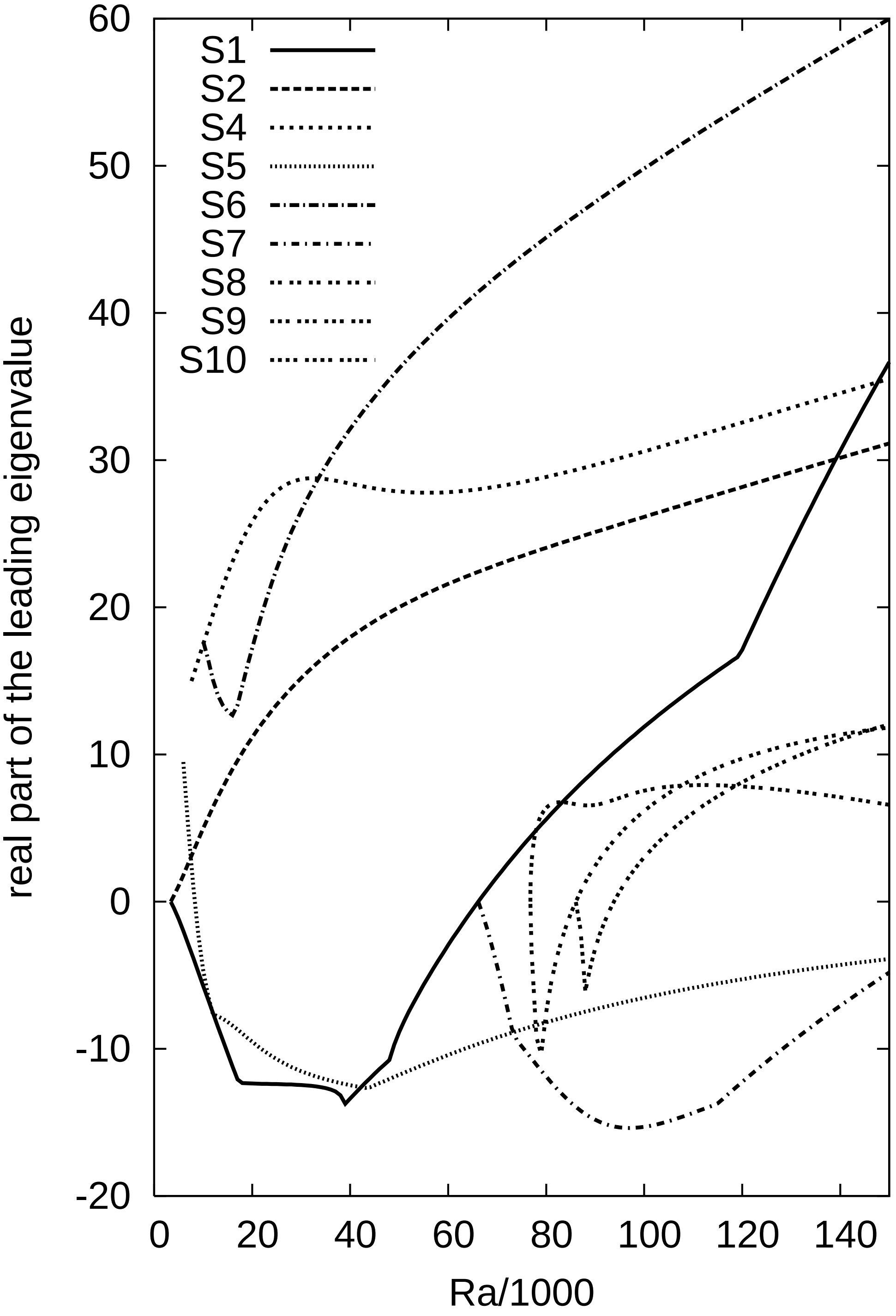

Figure 4: The real part of the leading eigenvalue is depicted as a function of $10^{-3}Ra$ for most of the flow patterns identified.

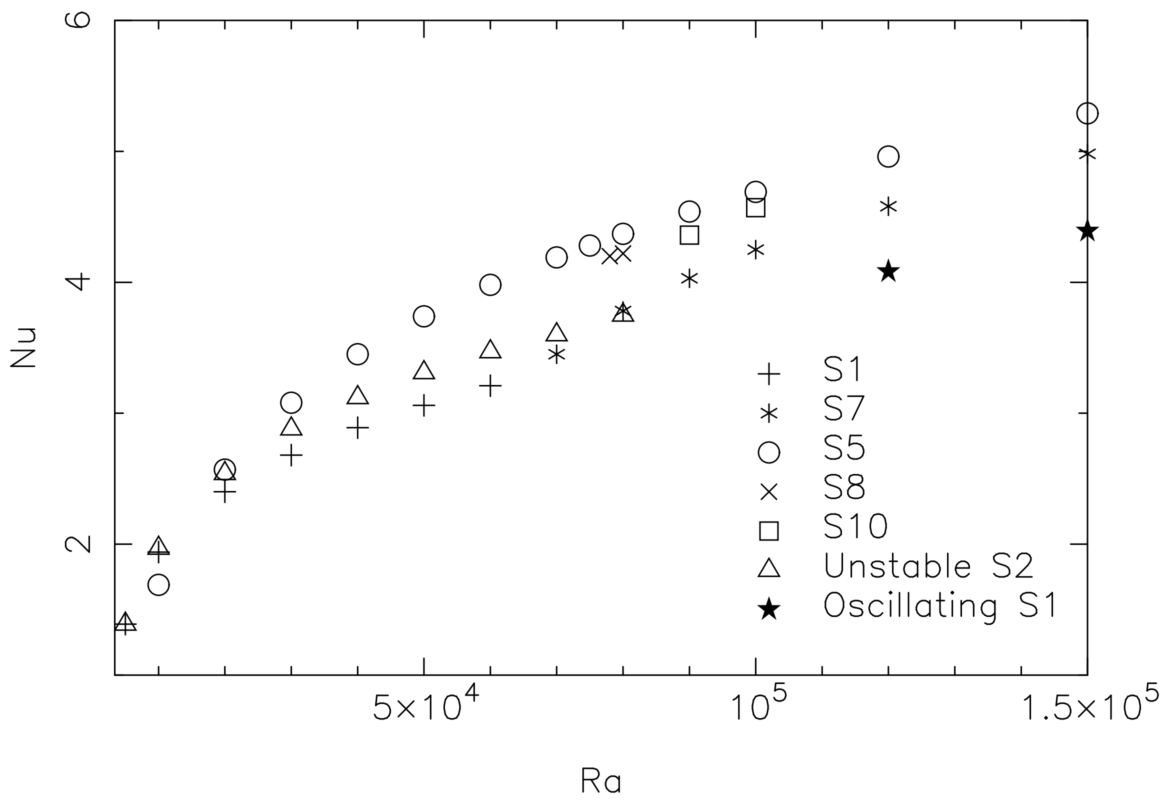

Figure 5: Numerical finite difference results. The Nusselt number Nu is depicted as a function of Ra at $Pr = 0.71$.

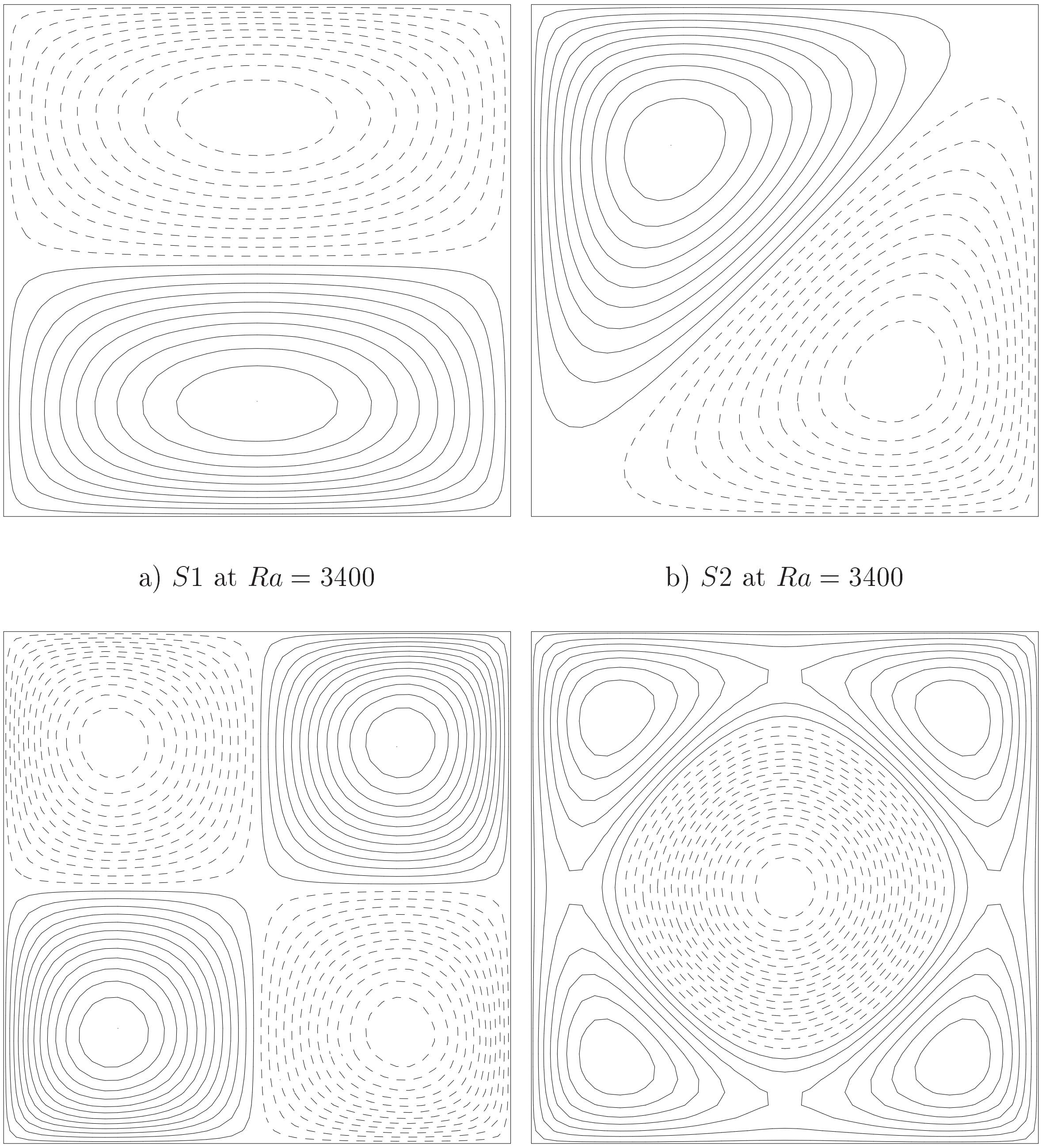

a) $S1$ at $Ra = 3400$

b) $S2$ at $Ra = 3400$

c) $S5$ at $Ra = 5950$

d) $S4$ at $Ra = 7600$

Figure 6: Vertical velocity contours in the horizontal midplane $z = 0$ for the flow patterns $S1$, $S2$, $S4$ and $S5$ at values of Ra slightly above the bifurcation points where they set in.

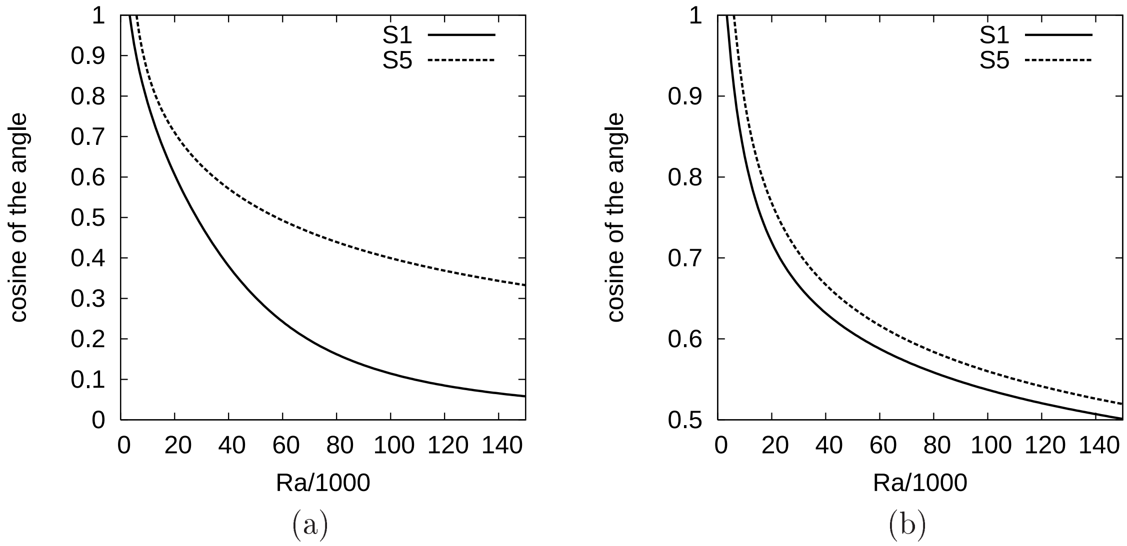

Figure 7: Variation with Ra of the cosine of (a) the angle between the solution of the nonlinear problem and the eigenvector associated with the leading eigenvalue predicted by equations linearized around the motionless conductive state for the single roll ($S1$) and the four rolls ($S5$), (b) the angle between the solution of the nonlinear problem and the corresponding solution at the bifurcation Rayleigh number where it sets in for the single roll ($S1$) and the four rolls ($S5$).

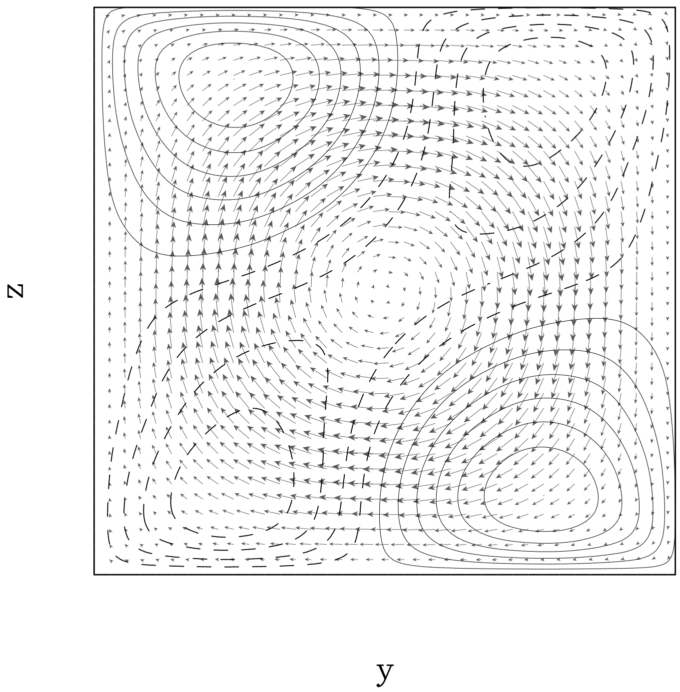

(a)

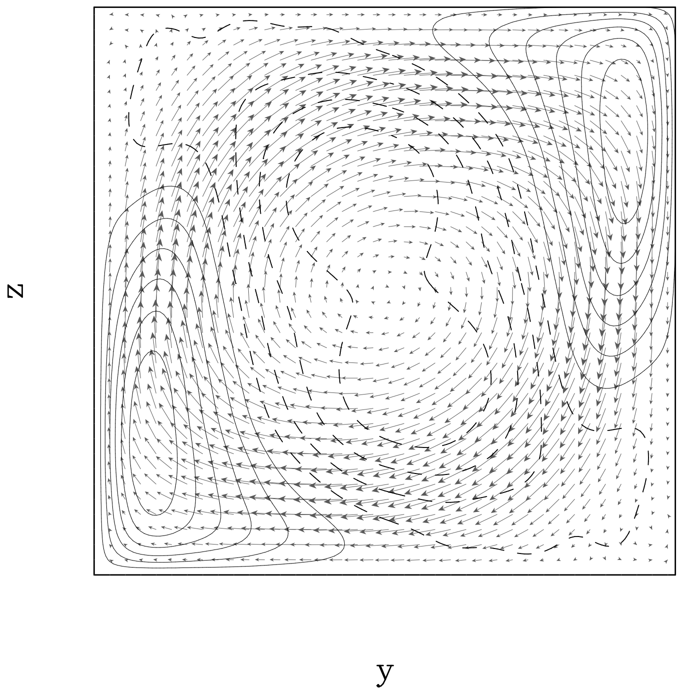

(b)

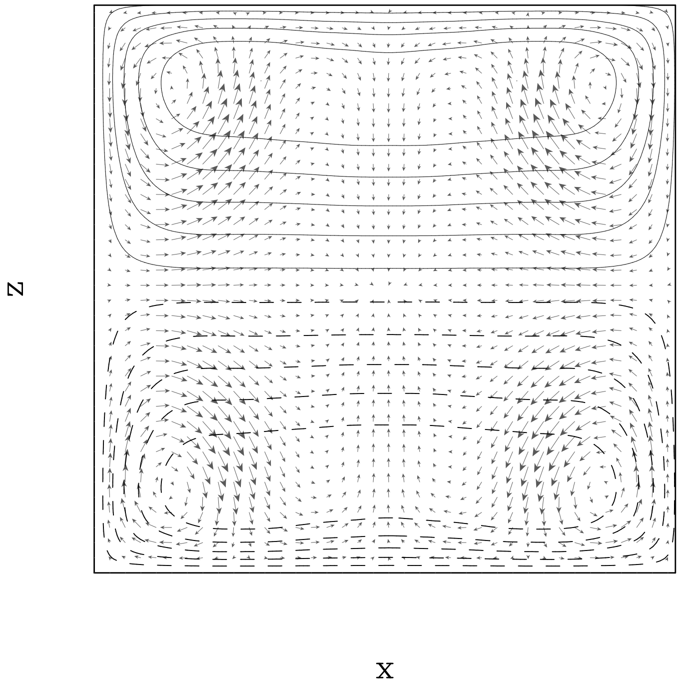

(c)

Figure 8: Contours of the velocity component normal to the vertical plane $x = 0.25$, together with the projected velocity vectors for the $S1$ flow pattern (x–roll) at (a) $Ra = 3,500$ and (b) $Ra = 50,000$. (c) The same type of plot for the vertical plane $y = 0$ at $Ra = 50,000$.

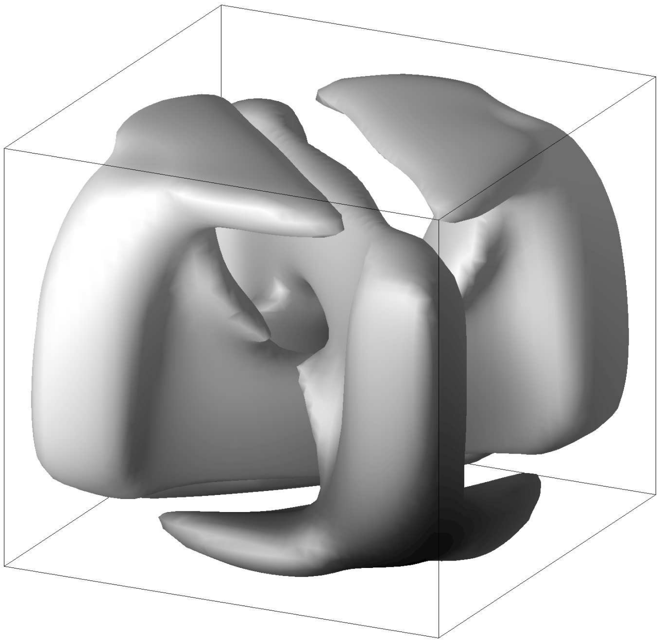

(a)

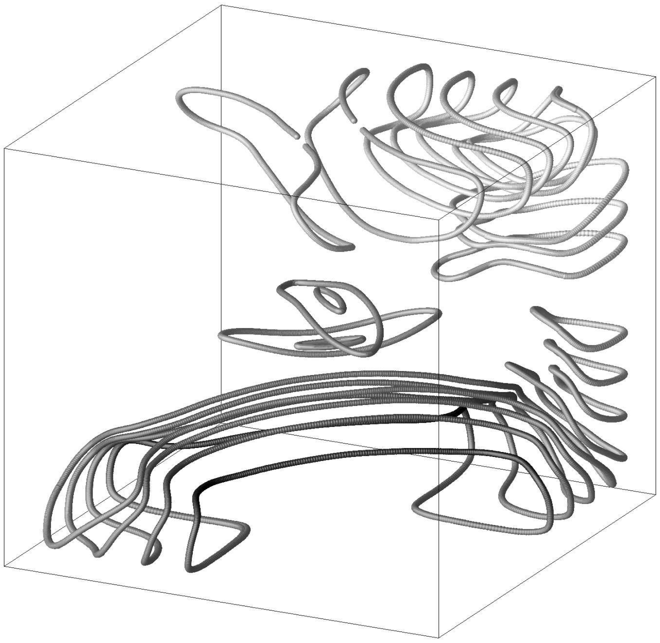

(b)

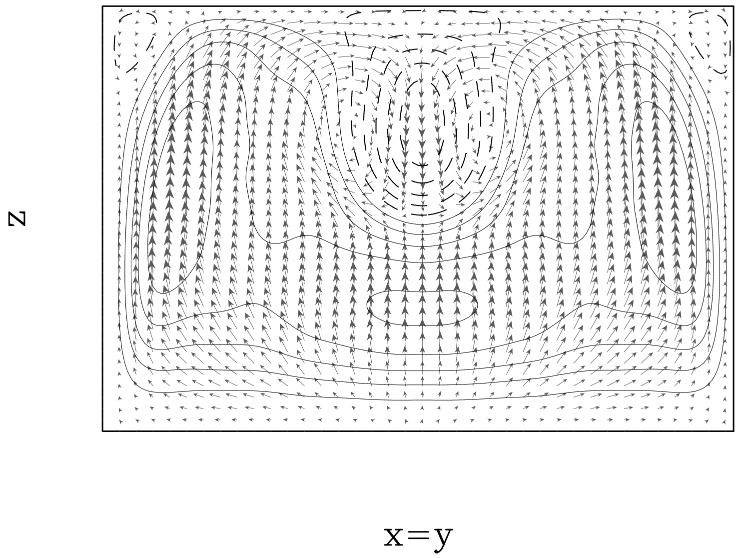

(c)

Figure 9: $S5$ flow pattern at $Ra = 1.5 \times 10^5$. (a) Isosurfaces of $\|\vec{V}\| = 0.18$. (b) Selected vortexlines denoting the shape of the vortical structure with upwelling motion along two vertical edges of the cavity. (c) Vertical velocity contours together with velocity vectors at the vertical diagonal plane $x = y$.

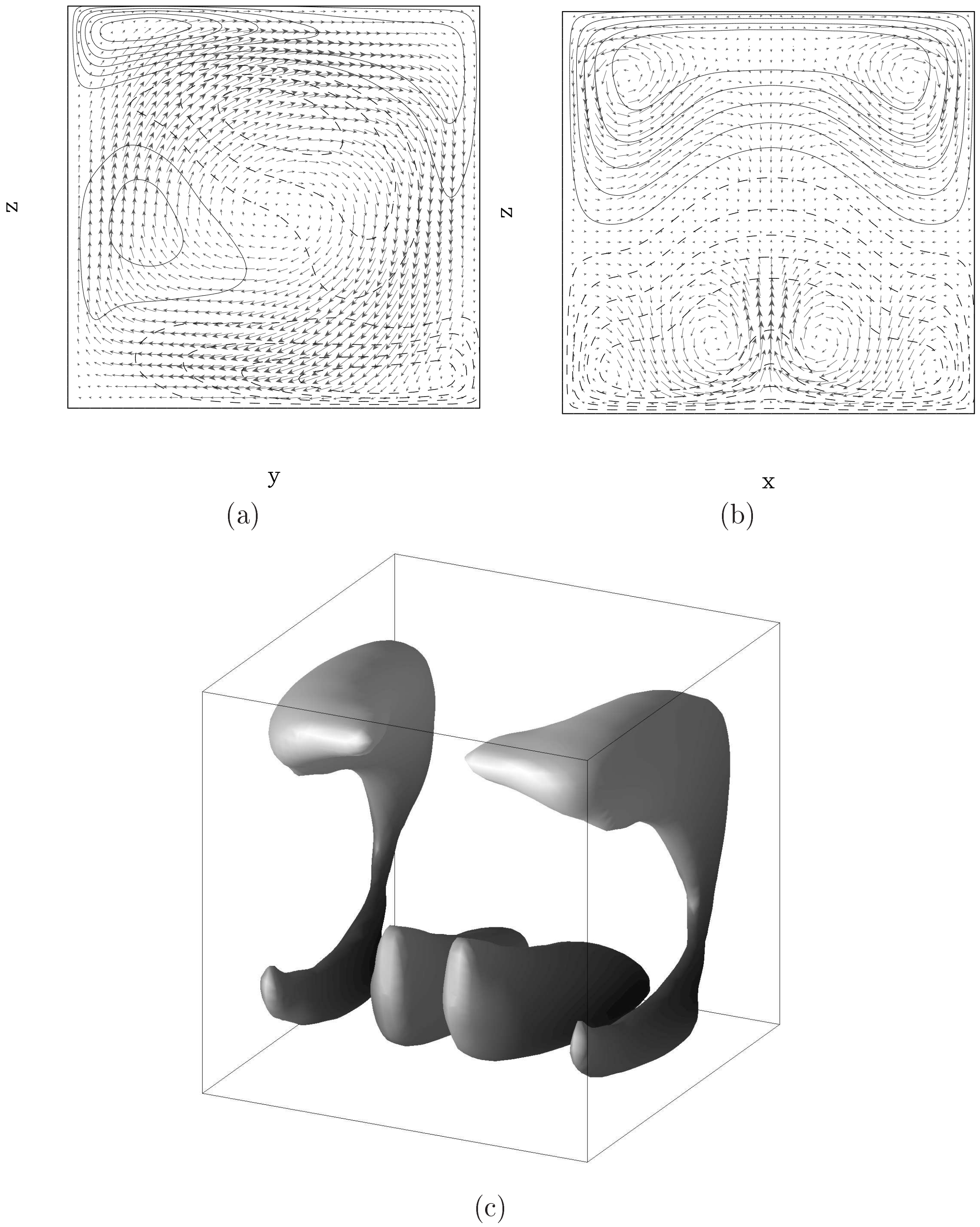

Figure 10: $S7$ flow pattern at $Ra = 10^5$. (a) Contours of the velocity component normal to the plane $x = 0.25$ together with the projected velocity vectors. (b) The same type of plot for the vertical plane $y = 0$. (c) Isosurfaces with helicity value $H = 0.083$.

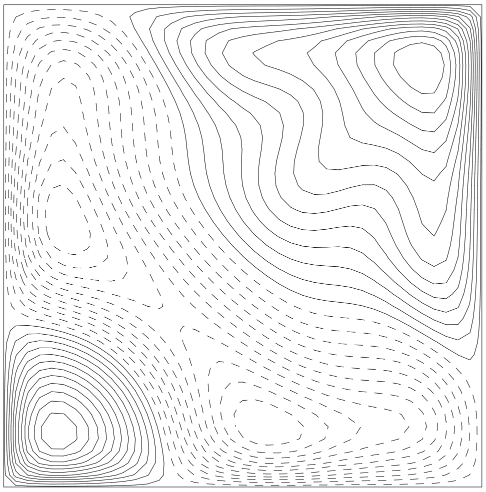

a1) $S8$ at $Ra = 80,000$.
Finite-difference results.

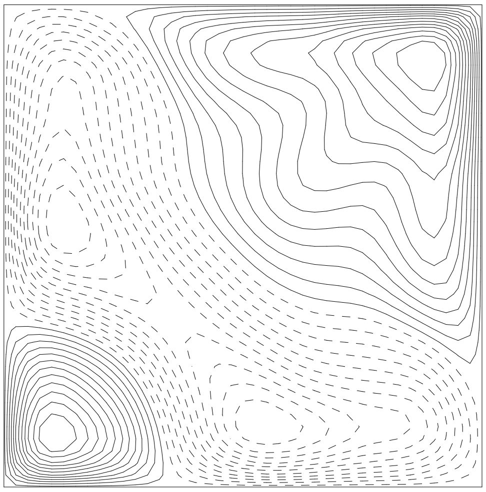

a2) $S8$ at $Ra = 80,000$.
Galerkin results.

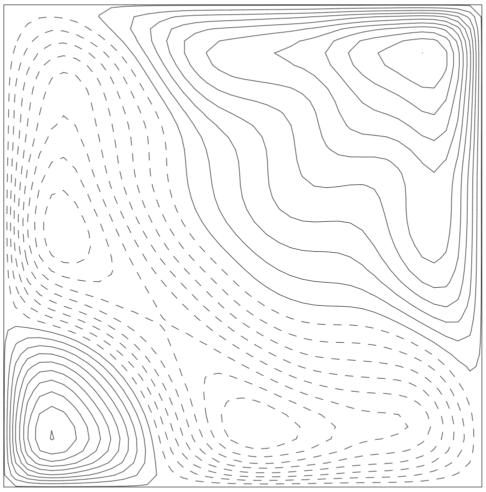

b1) $S10$ at $Ra = 87,000$

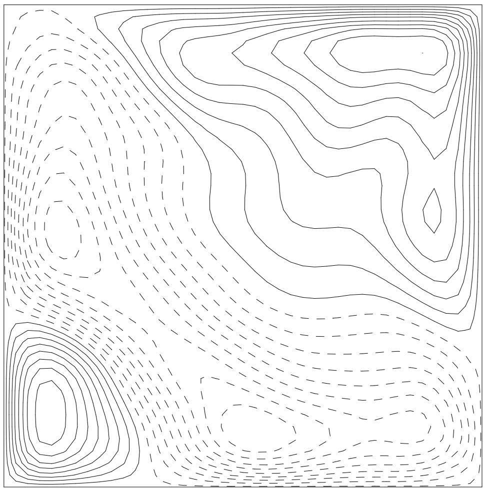

b2) $S10$ at $Ra = 1.2 \times 10^5$

Figure 11: Vertical velocity contours in the horizontal midplane $z = 0$ for the $S8$ flow pattern at $Ra = 80,000$ obtained (a1) by the finte-difference method and (a2) by the Galerkin method. The same kind of plot for the $S10$ flow pattern obtained by the Galerkin method at (b1) $Ra = 87,000$ and (b2) $Ra = 1.2 \times 10^5$.

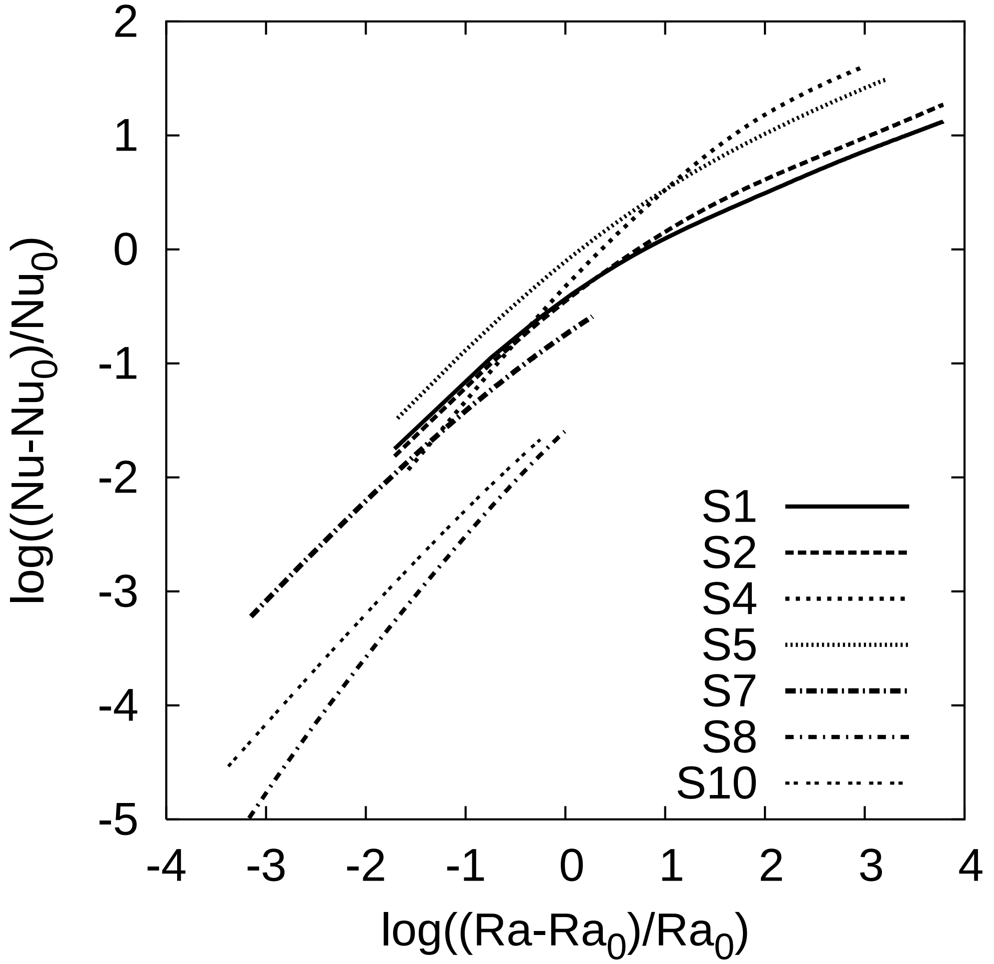

Figure 12: Variation of $\log\left(\frac{Nu-Nu_0}{Nu_0}\right)$ as a function of $\log\left(\frac{Ra-Ra_0}{Ra_0}\right)$ for most of the flow patterns identified. Here Ra_0 represents the value of the bifurcation Rayleigh number where a solution sets in and Nu_0 the corresponding value of the Nusselt number.

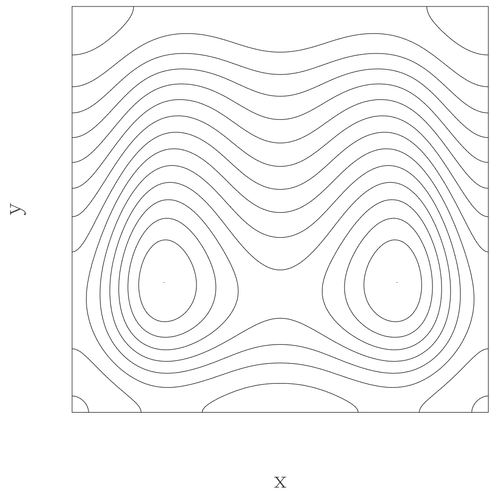

(a)

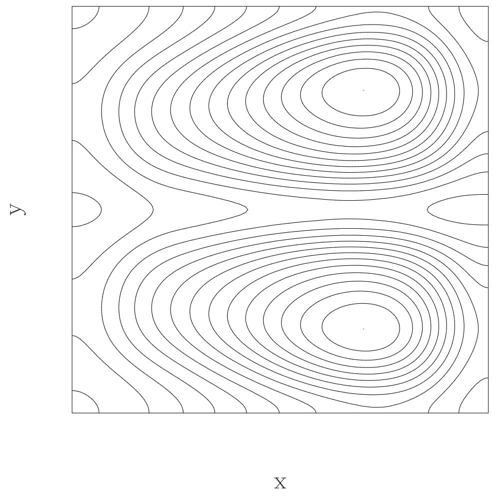

(b)

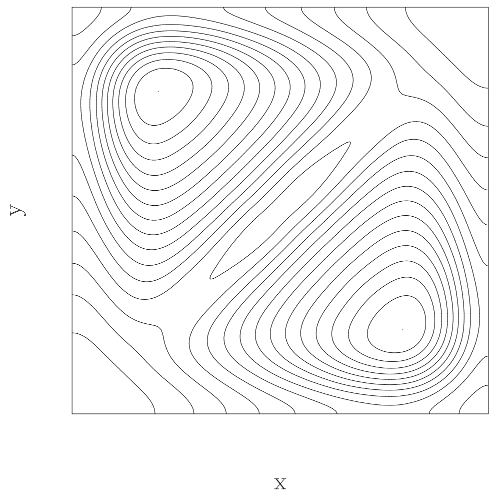

(c)

Figure 13: Distribution of the local Nusselt number at the bottom wall of the cavity for (a) $S1$ pattern at $Ra = 60,000$; (b) $S7$ pattern at $Ra = 10^5$; and, (c) $S5$ pattern at $Ra = 1.5 \times 10^5$.